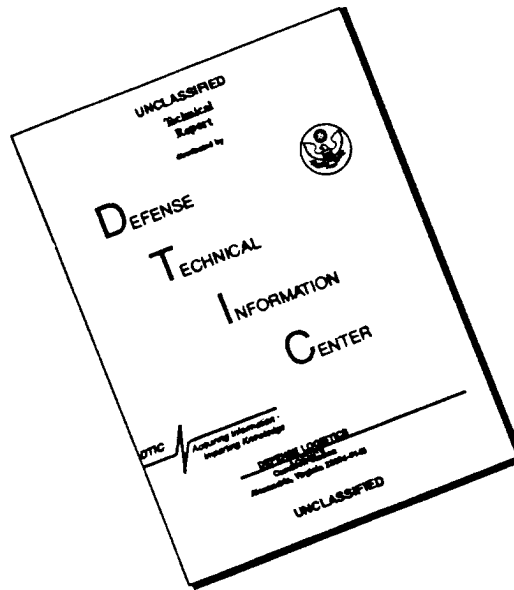


REPORT DOCUMENTATION PAGE			Form Approved OMB No. 0704-0188	
<small>Public reporting burden for this collection of information is estimated to average 1 hour per response, including the time for reviewing instructions, searching existing data sources, gathering and maintaining the data needed, and completing and reviewing the collection of information. Send comments regarding this burden estimate or any other aspect of this collection of information, including suggestions for reducing this burden, to Washington Headquarters Services, Directorate for Information Operations and Reports, 1215 Jefferson Davis Highway, Suite 1204, Arlington, VA 22202-4302, and to the Office of Management and Budget, Paperwork Reduction Project (0704-0188), Washington, DC 20503.</small>				
1. AGENCY USE ONLY (Leave blank)	2. REPORT DATE 5/30/96	3. REPORT TYPE AND DATES COVERED Final Technical 3/1/91--2/29/96		
4. TITLE AND SUBTITLE  (U) Free-stream Turbulence Effects on Stagnation Point Turbulence and Heat Transfer		5. FUNDING NUMBERS PE - 61102F PR - 2308 SA - BS G - AFOSR-91-0198-D		
6. AUTHOR(S)  Sanjiva K. Lele and Sungwon Bae		AFOSR-TR-96 0363		
7. PERFORMING ORGANIZATION NAME(S) AND ADDRESS(ES) Department of Mechanical Engineering Stanford University Stanford, California 94305-4035				
9. SPONSORING/MONITORING AGENCY NAME(S) AND ADDRESS(ES) AFOSR/NA 110 Duncan Avenue, Suite B115 Bolling AFB, DC 20332-0001		10. SPONSORING/MONITORING AGENCY REPORT NUMBER AFOSR 91-0198		
11. SUPPLEMENTARY NOTES				
12a. DISTRIBUTION/AVAILABILITY STATEMENT  Approved for public release; distribution is unlimited			12b. DISTRIBUTION CODE  19960726 070	
13. ABSTRACT (Maximum 200 words)  Stagnation point flow and heat transfer under free-stream turbulence was studied. A new code and an optimized scheme were developed for this study. The optimized scheme was found to significantly save the computational cost. In addition, methods for prescribing realistic inflow turbulence were developed. Simulations with organized inflow disturbances were conducted to study the effect of spanwise length scale and intensity on the enhancement of wall heat transfer and skin friction. Three regimes were identified depending on the spanwise length scale, "damping", "attached amplifying", and "detached amplifying" regimes. In the attached amplifying regime the enhancement of skin friction and heat transfer increases with the intensity of the inflow disturbance, but saturates for larger spanwise length scales. In all cases studied the heat transfer enhancement was 4-5 times larger than the skin friction enhancement. Finally, direct numerical simulations (DNS) of stagnation point flow with moderate grid resolution were conducted to study turbulence statistics. Mean profiles of $u$ velocity and temperature were compared with laminar profiles, and the statistics of turbulence kinetic energy were obtained. The simulations have not completed yet, and preliminary results are included in this report.				
14. SUBJECT TERMS  stagnation point heat-transfer, free-stream turbulence, direct numerical simulation			15. NUMBER OF PAGES 35	
			16. PRICE CODE	
17. SECURITY CLASSIFICATION OF REPORT Unclassified	18. SECURITY CLASSIFICATION OF THIS PAGE Unclassified	19. SECURITY CLASSIFICATION OF ABSTRACT Unclassified	20. LIMITATION OF ABSTRACT UL	

# DISCLAIMER NOTICE



THIS DOCUMENT IS BEST QUALITY AVAILABLE. THE COPY FURNISHED TO DTIC CONTAINED A SIGNIFICANT NUMBER OF PAGES WHICH DO NOT REPRODUCE LEGIBLY.



**Department of AERONAUTICS and ASTRONAUTICS  
STANFORD UNIVERSITY**

Final Technical Report on  
**Free-stream Turbulence Effects  
on Stagnation Point Turbulence and Heat Transfer**

for the peiord 3/1/91-2/29/96

by

Sanjiva K. Lele and Sungwon Bae  
Department of Mechanical Engineering  
Stanford University, Stanford, CA 94305-4035

Supported by

**Air Force Office of Scientific Research**

under grant AFOSR-91-0198-D  
Contract Monitor Dr. J. McMichael

# FINAL REPORT

## Numerical Simulation of Stagnation Point Flow and Heat Transfer under Free-Stream Turbulence

Sanjiva K. Lele  
Sungwon Bae

Department of Mechanical Engineering  
Stanford University

### Summary

Stagnation point flow and heat transfer under free-stream turbulence was studied. A new code and an optimized scheme were developed for this study. The optimized scheme was found to significantly save the computational cost. In addition, methods for prescribing realistic inflow turbulence were developed. Simulations with organized inflow disturbances were conducted to study the effect of spanwise length scale and intensity on the enhancement of wall heat transfer and skin friction. Three regimes were identified depending on the spanwise length scale, “damping”, “attached amplifying” and “detached amplifying” regimes. In the attached-amplifying regime the enhancement of skin friction and heat transfer increases with the intensity of the inflow disturbance, but saturates for larger spanwise length scales. In all cases studied the heat transfer enhancement was 4-5 times larger than the skin friction enhancement. Finally, direct numerical simulations (DNS) of stagnation point flow with moderate grid resolution were conducted to study turbulence statistics. Mean profiles of  $u$  velocity and temperature were compared with laminar profiles, and the statistics of turbulence kinetic energy were obtained. The simulations have not completed yet, and preliminary results are included in this report.

## 1 Introduction

Free-stream turbulence is known to influence wall heat transfer significantly. Simonich and Bradshaw (1978) showed that the free-stream turbulence enhanced wall heat transfer and skin friction in a flat plate boundary layer. Hancock & Bradshaw (1983) later proposed a scaling factor which is a function of the intensity and the integral length scale of the free-stream turbulence to account for these changes. As the intensity increased the enhancement of skin friction and wall heat transfer increased, but the length scale showed a reverse trend: as the length scale decreased the enhancement increased. They attributed this to a “blocking effect” of the wall on the large scale energy-containing eddies.

The flow near a stagnation point is much more susceptible to the effects of the free-stream turbulence than a canonical flat plate boundary layer. Kestin (1966) reported the enhancement of wall heat transfer rate by more than 100% for some cases. Suter (1965) attributed this enhancement to the amplification of vorticity in the flow approaching the stagnation

point. He proposed that only the disturbances with the spanwise length scale larger than the neutral scale which depends on the laminar boundary layer thickness, are amplified. The amplified vorticity disturbs a boundary layer significantly, causing the enhancement in skin friction and heat transfer.

A typical example of stagnation point flow with free-stream turbulence is the leading edge region of a turbine blade which is subjected to intense heat loads due to the impinging free-stream turbulence. The flow exiting a gas turbine contains high levels of turbulence. As this flow passes over the first stage blade of the turbine, high levels of heat transfer occur. Ames (1990, 1994) conducted experiments where flow from a mock combustor convected toward the first stage blades of a turbine, and showed that the leading edge heat transfer was enhanced significantly. He scaled the wall heat transfer results with the length scale and intensity of the flow from the mock combustor. It has been noted (Traci & Wilcox, 1975) that the effects of free-stream turbulence need to be incorporated in the turbulence models for engineering flow predictions. Calculations carried out without accounting for free-stream turbulence usually encounter difficulties in predicting the skin friction and heat transfer. Understanding the mechanism responsible for the enhancements by the free-stream turbulence is one step toward a better turbulence modelling.

Experiments have shown that wall heat transfer is more sensitive to free-stream turbulence than skin friction. Blair (1983) showed that the Reynolds analogy factor ( $2St/C_f$ ) increases in a flat plate boundary layer as the intensity of the free-stream turbulence increases (e.g. the free-stream turbulence intensity of 6% increases the Reynolds analogy factor by 7%.) Similar trend has been observed in the stagnation point flow, but with generally larger increase in the Reynolds analogy factor than for the flat plate boundary layer. Accurate modelling of such effects requires detailed knowledge of the flow in the stagnation point region.

The current project is a detailed study of the effects of free-stream turbulence on the stagnation point flow turbulence and heat transfer by numerical simulations of the flow. Two types of simulations are carried out, a) direct numerical simulations (DNS) of the stagnation point boundary layer with free-stream turbulence and b) simulations involving organized inflow disturbances.

## 2 Numerical Method

A new code was developed which uses fourth order spatial differencing scheme and second order implicit time advancement scheme. Fully implicit time advancement scheme is used to overcome the small time step restriction of explicit time advancement schemes. The inversion of sparse matrix associated with the fully implicit time advancement is carried out by line successive overrelaxation (LSOR) and small core memory in computation is managed by using plane SSD data base structure. The code is highly vectorized and has been validated by comparing with the Hiemenz flow (laminar stagnation point flow) and the evolution of isotropic decaying turbulence simulated by an already validated code.

Non-reflecting boundary condition (Giles, 1988) is used at both inflow and outflow boundaries and "Exit Zone" is appended to the outflow boundary to attenuate any disturbances reaching the outflow boundary. The Exit Zone (Colonius et al, 1993) is the region where the grid is stretched to attenuate the flow and thermodynamic disturbances, and a fourth order explicit filtering scheme is used to damp the unresolved flow features. The grid stretching and filtering are applied only within the Exit Zone; good solution accuracy is maintained in the domain outside the Exit Zone. No slip condition and isothermal condition,  $T_w/T_\infty = 0.8$  are imposed at the wall, where  $T_w$  and  $T_\infty$  denote the temperature of the wall and free-stream respectively.

## 2.1 Optimized scheme

An optimized scheme was developed to enhance the high wave number representation in the computation of spatial derivatives. Figure 1(a) shows the modified wave numbers,  $k_{m1}$  of four different schemes. The optimized scheme shows better high wave number representation than the fourth order central differencing scheme, and is slightly less accurate than the sixth order central differencing scheme (Figure 1(b)). Since both the optimized scheme and the fourth order central differencing scheme use a 5 point stencil, the computational cost of the both schemes are same. The sixth order central differencing scheme uses a 7 point stencil and the Pade scheme (sixth order implicit scheme) requires matrix inversion so that their computational cost is higher than the other two explicit schemes considered in Figure 1(a).

Figure 1(b) shows the error in the wave number representation for each scheme. The curves of the fourth order central differencing scheme, the sixth order central differencing scheme and Pade scheme show similar trend: the higher the wave number the larger is the magnitude of the error. However, the  $k_{m1}$  of the optimized scheme shows an overshoot (local maximum at  $kh = 0.86$ ). This overshoot allows the optimized scheme to have a wider range of wave numbers which have less error ( $(k_{m1} - k)/k \leq \epsilon$ ) than the fourth order central differencing scheme. The error tolerance  $\epsilon = 0.022$  was used for the optimized scheme of this example. The sixth order compact scheme shows the best wave number representation, and is chosen to be the reference scheme when evaluating the results computed with other schemes. The same method was also applied to the evaluation of second order derivative. Figure 2(a) and 2(b) show the modified wave number representation and the error in the wave number representation for each scheme.

To assess the performance of the optimized schemes in simulating turbulent flows, computations of isotropic decaying turbulence were conducted. Table 1 shows the number of grid points used with different schemes and the initial Taylor microscale Reynolds number ( $Re_{\lambda_0}$ ) for each case. Figure 3 shows the decay of the turbulent kinetic energy obtained with different schemes against nondimensional time (time is normalized by the flow turn-over time,  $\tau = \frac{\sqrt{q_i^2/3}}{l_i}$ , where  $q_i^2$  is initial value of  $q^2 (= \overline{u'^2} + \overline{v'^2} + \overline{w'^2})$  and  $l_i$  is initial Taylor microscale). All four curves collapse to almost one curve. This is attributed to the fact that the turbulent kinetic energy depends mostly on the large-scale eddies which are associated with the low wave numbers. Since all four schemes resolve the low wave numbers sufficiently,

the statistics do not show much difference. This also verifies that the overshoot in the modified wave number of the optimized scheme does not significantly affect the turbulent kinetic energy. Figure 4 shows the time evolution of mean square vorticity. Since vorticity depends on the spatial derivatives of the velocity field, its statistics are more dependent on the higher wave numbers than the turbulent kinetic energy. In fact, the curve of Scheme 4 (optimized scheme) is closer to the curve of Scheme 1 which provides the best representation of the high wave number among the four schemes, than the curve of Scheme 3. Figure 5 shows the time evolution of velocity derivative skewness which also depends highly on the contributions from the high wave numbers. Unlike figure 4, Scheme 3 shows better results than Scheme 4. This is attributed to the fact that the range of the wave numbers influencing the skewness are higher than the wave numbers influencing mean square vorticity.

It was concluded that the results from Scheme 4 scheme are superior to the results from Scheme 2 and comparable to the results from Scheme 3. With the implicit time advancement the computational cost of Scheme 3 (which uses a  $120^3$  mesh) is  $1.5^3 (=3.375)$  times larger than Scheme 4 (which uses a  $80^3$  mesh). The optimized scheme was found to yield results comparable with fourth order central differencing scheme with  $1.5^3$  times as many grid points; the savings in computational cost with the optimized scheme are significant.

## 2.2 Generation of Inflow Turbulence

Stagnation point flow is sensitive to the characteristics of the free-stream turbulence, among which the intensity and the length scale have been reported to play a key role in the enhancement of the wall heat transfer and the skin friction coefficient. It is, therefore, critical to establish that the algorithms used in the DNS of stagnation point flow, yield physically reasonable inflow turbulence. The free-stream turbulence is idealized as homogeneous isotropic turbulence akin to grid-generated turbulence in an experiment. This idealized inflow is then subjected to the deformation of the mean strain rate as it convects from the inflow boundary toward the boundary layer.

Two different methods of prescribing the turbulent inflow disturbances were evaluated (a schematic of the stagnation point flow is given in Figure 26, where the coordinate axes are labelled.) Method 1 is to supply the inflow data from the results of a precomputed field of homogeneous and isotropic turbulence (the computational domain for isotropic turbulence calculation is the same in  $y - z$  plane as that in Figure 26 except that  $y$  is another homogeneous direction with the same mesh size as  $z$ .) The computational domain in  $x$  direction is, however, much longer for the simulation of the stagnation point flow. The isotropic turbulence field is periodically extended in  $x$  direction to supply the inflow turbulence over its whole inflow plane. Figure 6 shows the  $w$  velocity contours of the inflow turbulence field where the periodic extension in  $x$  direction is evident.

Method 2 is to supply the results of the homogeneous and isotropic turbulence conducted on the same computational domain as the simulation of the stagnation point flow. Non-uniform grid is used in  $x$  direction which matches the target grid for the stagnation point flow. A uniform grid in  $x$  direction is unnecessary because only eddies near the center of the

inflow boundary are convected to the boundary layer and play a significant role in changing of the wall heat flux and skin friction. Flow near the edge of the inflow boundary simply convects to the outflow boundary, never reaching the boundary layer. This justifies the use of Exit Zone. The starting position of Exit Zone is  $0.5L_x$  where  $L_x$  is the half domain size in the  $x$  direction. Figure 8 shows the  $w$  velocity contours of the inflow turbulence field, and damping of the turbulence in the Exit Zone is evident.

Method 1 maintains isotropy and homogeneity of the inflow turbulence, but suffers from poor statistical sample of the large eddies. This is evident in Figure 6 and 7. Figure 6 shows  $w$  velocity contours from a stagnation point DNS supplied with the inflow turbulence using Method 1. Figure 7 shows the streamwise vorticity contours at different distances from the wall. Even at  $y/\delta = 3$ , significant periodicity is evident. Method 2 yields a larger number of statistically independent samples than Method 1. As shown in Figure 8, no periodicity is noticed in the field. To establish the degree to which the homogeneity and isotropy are maintained in Method 2, turbulence statistics averaged in  $y$  and  $z$  directions are plotted against  $x$  coordinate. Figure 9 shows the variation of diagonal terms of the anisotropy tensor,  $b_{ij}$ , defined as

$$b_{ij} = \frac{\langle u'_i u'_j \rangle}{\langle u'_k u'_k \rangle} - \frac{1}{3} \delta_{ij}$$

against  $x$  direction.

For homogeneous and isotropic turbulence,  $b_{11} = 0, b_{22} = 0$  and  $b_{33} = 0$ . For  $-0.5 \leq x/L_x \leq 0.5$ , the plots of  $b_{\alpha\alpha}$  show quasi-homogeneity and quasi-isotropy. The 'fluctuations' reflect the small sample size available when averaging over  $y-z$  planes. Figure 10 shows the variation of the velocity derivative skewness with  $x$  coordinate. The statistics are isotropic and homogenous in the 'central' region, but become anisotropic and inhomogeneous in the region of grid non-uniformity. The degree of inhomogeneity and anisotropy is more noticeable than for the Reynolds stress anisotropy. This is attributed to the fact that the statistics of the velocity derivative skewness are dependent more on high wave numbers. Fine grid DNS of stagnation point flow will use Method 2.

### 3 Direct Numerical Simulations with Organized Disturbances

To assess the impact of inflow disturbances on the stagnation point flow, simulations with organized disturbances were carried out. Streamwise vorticity is prescribed at the inflow boundary by adding a spanwise periodic disturbance to the normal component of mean velocity at inflow boundary ( $v_{mean}$ ). The disturbance is of the form:

$$v(x, z) = v_{mean}(x, z) (1 + A_{org} \sin(2\pi z / \lambda_{org}))$$

$A_{org}$  denotes the "intensity" and  $\lambda_{org}$  sets the spanwise length scale of the perturbation.

Cases (tabulated in Table 3) with different intensities, length scales and Reynolds number were run. The Reynolds number is based on the laminar boundary layer thickness,  $\delta$ .



Another Reynolds number based on a characteristic length scale  $L$  is also shown in Table 3.  $L$  is defined as  $V_\infty/S$  where  $V_\infty$  is the free-stream velocity and  $S$  is mean strain rate. Note that cases labelled with \* denote damping cases according to Suter (1965). Figure 11 shows a schematic diagram of the simulations with organized disturbances.

Figure 12 shows the particle traces and the temperature field for the case L5I25 (which corresponds to  $\lambda_{org}/\delta = 5.3$  and intensity = 25%). It is clear that the organized disturbance changes the structure of the flow and temperature field. The particle traces reveal a periodic array of counter-rotating streamwise vortices whose cores reside near the edge of the laminar boundary layer. A similar structure is also observed in a flat plate boundary layer (Sabry & Liu, 1991). The temperature contours show the distortion due to the fluid motion induced by counter-rotating streamwise vortices. At the location where the vortices induce upwash motion, a mushroom-shaped low temperature region is found. On the other hand, isotherms are pushed towards the wall at downwash locations. The increased temperature gradient in the downwash regions results in an overall wall heat transfer increase.

The spanwise distribution of skin friction ( $C_f$ ) and Stanton number ( $St$ ), and their mean value were studied as a function of the length scale and intensity of the inflow disturbances. Three regimes are identified which depends on the spanwise length scale: “damping” regime, “attached amplifying” regime and “detached amplifying” regime. These are best illustrated by the behavior of the streamwise vorticity. Figure 13 shows the contours of the streamwise vorticity for these three typical cases. When the spanwise length scale is smaller than a critical length scale, the disturbance is damped (Suter, 1965). Accordingly, in Figure 13(a) the streamwise vorticity contours are monotonically damped away from the inflow boundary. The opposite signed vorticity at the wall is the results of the no slip boundary condition. The cases shown in Figure 13 (b),(c) correspond to the amplifying regime. These are found to follow two distinct patterns. In the “attached amplifying” regime (illustrated in Figure 13(b)), the vorticity peak is located near the edge of the boundary layer. This flow pattern is found to occur for moderate spanwise length scales. However, when the spanwise length scale is larger, the streamwise vorticity detaches itself from the boundary layer, rolls up into strong vortex cores and equilibrates at a larger distance from the wall. This is shown in Figure 13(c): note the large vorticity magnitude and the detachment of the vortex cores from the boundary layer.

The simulations show that the impact of the inflow disturbances on the skin friction and wall heat transfer depends on flow regime corresponding to the spanwise length scale of the disturbance. The near wall behaviors in the “attached amplifying” and “detached amplifying” regimes are described in the following sections.

### 3.1 Near wall behavior in “attached amplifying” regime

The deviation of  $C_f$  from its laminar value ( $\Delta C_f$ ) is plotted against the spanwise direction in Figure 14. The vertical axis represents  $\frac{\Delta C_f}{C_{f,laminar}} * 100$ , (i.e. the percent change of  $C_f$  from the laminar  $C_f$ .) Two trends are noted in the figure. First, the higher the intensity, the larger is the deviation, and this trend is preserved for all three length scales. Additionally, this

trend is consistent with the trends of previous experimental studies by others. Second, as the spanwise length scale increases (from  $3.2\delta$  to  $4.0\delta$ ),  $C_f$  increases too, but the increase is not noticeable when the length scale is increased from  $4.0\delta$  to  $5.3\delta$ . This suggests that  $\Delta C_f$  tends to saturate as the length scale increases more. The shape of the  $\Delta C_f$  curves deviates from the sinusoidal form as the intensity increases, and the region of the positive  $\Delta C_f$  increases with the intensity. Consequently, when the  $\Delta C_f$  is averaged over the  $z$  direction to obtain  $\overline{\Delta C_f}$ , the mean change in  $C_f$  increases with intensity. As the length scale increases further so that the “detached amplifying” regime is attained, the  $\Delta C_f$  decreases, implying that there is a length scale which maximizes  $\Delta C_f$  for a given intensity and Reynolds number. Experiments have reported that the length scale is inversely correlated with  $\overline{\Delta C_f}$ . This is attributed to the fact that the range of length scale of the free-stream turbulence used in the experiments corresponds to the “detached amplifying” regime. Table 2 shows the ranges of length scales associated with inflow turbulence from some recent experiments. The experiments report either integral length scale related to the large energy containing eddies or the dissipation length scale defined as  $\epsilon/u'^3$  where  $\epsilon$  is dissipation. Therefore, it is evident that the ranges of length scale used in experiments are higher than those which yield the “attached amplifying” regime.

The deviation of  $St$  from its laminar value ( $\Delta St$ ) is plotted against the spanwise direction in Figure 15. The general trends found in the plot of  $\Delta C_f$  also apply to  $\Delta St$ . However, some differences are worth noting. The maximum  $\Delta St$  is higher than the maximum  $\Delta C_f$  for the same inflow disturbance parameters, and so is the minimum  $\Delta St$ . For the case of L4I25, the maximum  $\Delta St$  increases up to 80% whereas the maximum  $\Delta C_f$  rises to 25%, and the minimum  $\Delta St$  decreases to -45% whereas the minimum of  $\Delta C_f$  falls to -15%. Therefore,  $\Delta St$  is more sensitive to the organized disturbances than  $\Delta C_f$ . Sutra (1963) reported a similar sensitivity in his model representing the effects streamwise vortices. The shapes of the curves of  $\Delta St$  also show more deviation from the sinusoidal form than  $\Delta C_f$ . The region associated with the positive  $\Delta St$  is larger than the region associated with the positive  $\Delta C_f$  deviation. This is consistent with  $\overline{\Delta St}$  being larger than  $\overline{\Delta C_f}$  for the same inflow disturbance.

### 3.2 Near wall behavior in “detached amplifying” regime

As the spanwise length scale is increased further,  $C_f$  and  $St$  decrease, which is consistent with experimental results. Figure 16 shows  $\Delta C_f$  and  $\Delta St$  for cases with  $Re_\delta = 240$ . As the length scale is increased from  $5.3\delta$  to  $10.3\delta$ , the maximum  $\Delta C_f$  decreases from 25% to 10% whereas the minimum value remains almost same. Likewise, the maximum  $\Delta St$  decreases from 130% to 70%.

The difference between “attached amplifying” and “detached amplifying” regimes is emphasized in Figure 17 where the spanwise peak of streamwise vorticity is plotted against the self-similar coordinate,  $\eta$  ( $= \frac{y}{\sqrt{S/\nu}}$  where  $S$  is mean strain rate and  $\nu$  is kinematic viscosity.) The streamwise vorticity in both cases is scaled by the inflow value. A peak vorticity value of almost 80 times the inflow value is attained in the latter case, while in the former case the peak value is only about 3 times the inflow value. Evidently, as the length scale is increased,

the streamwise vorticity rolls up into a strong vortex core and is further stretched by the mean flow. The distance of the peak streamwise vorticity from the wall is plotted against time in Figure 18(a). The distance,  $h$  is scaled by  $\sqrt{S/\nu}$ . The streamwise vortices are convected from the inflow boundary to the edge of the boundary layer by  $\text{Time} = 5$ , move away from the boundary layer later, and finally reach a quasi-steady location. Consequently, the skin friction and the wall heat transfer rate increase to maximum values, and then decrease to steady values as the vortices move to a steady location. The effect of this “detached” streamwise vorticity on the enhancement of the skin friction and wall heat transfer is shown in Figure 18(b) where the time evolution of the mean changes in skin friction  $\overline{\Delta C_f}$  and mean wall heat transfer  $\overline{\Delta St}$  is plotted. As the vortices move farther away from the wall, although their strength grows, their impact on the skin friction and wall heat transfer diminishes. The decrease in the enhancement of the skin friction and wall heat transfer with increasing length scale has been reported by many experiments (Ames, 1990 & 1994; Van Fossen et al, 1995; Blair 1983.) The present simulation provide an explanation of why this is so.

Table 3 shows values of  $\overline{\Delta C_f}$ ,  $\overline{\Delta St}$ ,  $H_v$ ,  $H_s$ ,  $L_v$ ,  $H_m$ ,  $v'_m/S\delta$ ,  $w'_m/S\delta$  and  $t'_m/\Delta T$  where subscript  $m$  represents maximum value. The schematic in Figure 11(b) defines various length scales:  $H_v$  is the distance of the streamwise vortices from the wall;  $H_s$  is the distance of the upper stagnation point from the wall;  $L_v$  is the distance between the two counter-rotating vortices inducing upwash motion;  $H_m$  is the distance of peak vertical velocity  $v'_m$  from the wall.  $\overline{\Delta C_f}$  and  $\overline{\Delta St}$  are percent values of the change relative to the laminar flow and  $H_v$ ,  $H_s$ ,  $L_v$  and  $H_m$  are given in terms of the similarity variable (note that 99% laminar boundary layer thickness is 2.4 in terms of the self-similar coordinate.) For all cases,  $\overline{\Delta St}$  is larger than  $\overline{\Delta C_f}$ , showing that  $St$  is more sensitive to the inflow disturbance than  $C_f$ . For L5I25,  $\overline{\Delta St}$  increases to 39% of its laminar value, while  $\overline{\Delta C_f}$  increases to 8% of its laminar value. Figure 19 shows  $\overline{\Delta C_f}$  vs.  $\overline{\Delta St}$  for all cases.  $\overline{\Delta C_f}$  is found to be linearly correlated with  $\overline{\Delta St}$  and the slope of the correlation has a value between 4.0 and 5.0. At low intensity (5-10%) the dynamics of vorticity amplification is linear and  $H_v$  scales with inflow spanwise length scale,  $\lambda_{org}$ . At higher intensity nonlinearity becomes important and the streamwise vorticity rolls up into a pair of vortices. The distance  $L_v$  between the pair is almost constant while their height  $H_v$  increases as the inflow length scale  $\lambda_{org}$  is increased. The peak vertical velocity induced by the vortices decreases as  $\lambda_{org}$  increases, which results in decreased  $\overline{\Delta C_f}$  and  $\overline{\Delta St}$ . In Figure 20(a)  $\overline{\Delta C_f}$  and  $\overline{\Delta St}$  are plotted against the peak vertical velocity,  $v'_m$ . The data points with  $v'_m/S\delta \leq 0.5$  appear to follow a  $(v'_m/S\delta)^2$  dependence. Such a scaling is expected based on linear vorticity amplification. For larger  $v'_m/S\delta$  there appears to be a break in the curve followed by a more gradual rise. The data points corresponding to the “detached amplifying” regime follow a trend close to  $(v'_m/S\delta)$ . Figure 20(b) shows the maximum in the temperature fluctuation against  $(v'_m/S\delta)$ . At small  $v'_m$ ,  $t'_m/\Delta T$  increases with  $v'_m$  and saturates to a maximum around 0.2.

### 3.3 Amplification of streamwise vorticity

To explore the mechanism responsible for the enhancement of the skin friction and wall heat transfer, the variation of the streamwise vorticity is examined. The streamwise vorticity of the inflow disturbance is stretched by the mean strain rate as the flow is convected toward the boundary layer. The magnitude of the streamwise vorticity reaches its peak value near the edge of the boundary layer. The vorticity changes its sign inside the boundary layer and reaches another peak value with an opposite sign at the wall. According to Suter (1965), there is a “neutral scale” which determines whether the streamwise vorticity is amplified or damped. This neutral scale is known to be approximately 10 times the displacement thickness of the laminar boundary layer. If the length scale of the streamwise vorticity is larger than the neutral scale, the vorticity is amplified whereas if the length scale is smaller than the neutral scale, the vorticity is damped.

Figure 21 confirms the existence of the neutral scale. The streamwise vorticity (at the position of its spanwise peak) for each case is plotted against the laminar self-similar coordinate,  $\eta$ . The streamwise vorticity is scaled by the inflow value. In the damping cases (L2I05) the streamwise vorticity is monotonically damped from the inflow boundary whereas in the amplifying cases (L3I25, L4I25, L5I25) the vorticity is amplified external to the laminar boundary layer and changes its sign inside the boundary layer. The laminar boundary layer thickness is approximately 2.4 in the self-similar coordinate, and cases with different length scales show peak vorticity at slightly different distances from the wall. The intensity of the inflow disturbance also affects the location and the magnitude of the peak streamwise vorticity. This is shown in Figure 22. The streamwise vorticity is scaled by the inflow value. Cases with  $l = 3.2\delta$  are plotted in Figure 22(a), and it is noted that curves of 5%, 10% and 25% inflow disturbance follow almost the same trend. Cases with higher length scale  $l = 5.3\delta$  are plotted in Figure 22(b), where the 5% and 10% disturbance cases are close to each other, but the curve of 25% shows a different trend. This suggests that the vorticity amplification process is linear in the former cases, but as the spanwise length scale and the intensity increase nonlinear effects become important. This explains why the enhancement of the skin friction and wall heat transfer saturates as the intensity of the inflow disturbance increases. Figure 23 shows the contours of streamwise vorticity for cases with different spanwise length scale,  $\lambda_{org}$ . The Reynolds number and intensity are held fixed. Figure 23(a) corresponds to the “attached amplifying” regime while Figure 23(b)-(d) are in the “detached amplifying” regime. As the spanwise length scale increases, the streamwise vorticity rolls up to form vortices of opposite sign, which move closer together as  $\lambda_{org}$  is further increased and form a vortex pair. The strength of the vortex pair decreases in the “detached amplifying” regime and its equilibrium distance from the wall increases: both of these reduce the peak vertical velocity induced by the vortex pair.

### 3.4 Scaling with Reynolds number and spanwise length scale

The effect of the Reynolds number is shown in Figure 24 where  $\Delta C_f$  and  $\Delta St$  obtained with inflow disturbance of fixed intensity of 25% and fixed length scale of  $5.3\delta$  for flows

at three different Reynolds number are plotted. As the Reynolds number increases,  $\Delta C_f$  and  $\Delta St$  increase. This is consistent with experimental results where Frössling number ( $Fr = Nu/\sqrt{Re_D}$  where  $Nu$  is Nusselt number, and  $D$  is a diameter) is often plotted against  $Tu$  (intensity) times  $Re_D^{0.5}$ .  $\Delta Fr$  has been reported to be correlated with  $Tu \cdot Re_D^n$ . Ames (1990,1994) used  $n = 5/12$ ; Van Fossen et al used  $n = 0.4$ ; Normally  $n = 0.5$  has been widely used. Figure 25(a) shows  $\Delta St/St_{lam}$  and  $\Delta C_f/C_{f,lam}$  where  $lam$  represents laminar value against  $Re_L$  where  $L$  is the characteristic length scale, in “detached amplifying” regime. The slope of the curve between  $Re_L = 10000$  and  $Re_L = 20000$  is found to be 0.37 approximately. The data associated with  $Re_L = 5000$  is not included in the calculation of the slope since it is in the “attached amplifying” regime. Therefore, it is found that the correlation between heat transfer rate and Reynolds number is consistent with experimental trends.

The effect of the length scale of the inflow disturbance is often combined with the intensity and Reynolds number when representing the wall heat transfer enhancement. A combined parameter  $Tu \cdot Re_D^n \cdot (l/D)^m$  is used where  $D$  is a diameter. Ames (1990, 1994) used  $m = -1/3$ ; Van Fossen et al. (1995) used  $m = -0.287$ . Figure 25(b) shows  $St/St_{lam}$  and  $C_f/C_{f,lam}$  against  $\lambda/\delta$  for cases with  $Re_\delta = 240$ . The slope of the curve for  $St$  is found to be -0.3 approximately, and this corresponds to  $m = -0.3$ .

To conclude, three distinguished regimes (characterized by the length scale) are found, “damping” regime, “attached amplifying” regime and “detached amplifying” regime. Each regime has a characteristic structure of the streamwise vorticity. In terms of the enhancement, the “attached amplifying” regime is the most effective. The qualitative dependence of  $\overline{\Delta C_f}$  and  $\overline{\Delta St}$  on Reynolds number and spanwise length scale observed with the organized inflow disturbances is consistent with the experimental findings in the turbulent flow regime.

## 4 Direct Numerical Simulation of Stagnation Point Flow with Free-Stream Turbulence

Two direct numerical simulations (DNS) with moderate grid resolution were performed. The focus of these simulations is on turbulence statistics in the stagnation point flow and heat transfer, which the simulations with organized disturbances (described in the previous section) can not provide. The simulations parameters were chosen to obtain different regimes in these simulations. First simulation (DNS1) uses Method 1 for inflow turbulence, and the length scale of the most energy containing eddies in the inflow turbulence is in the “damping” regime. Second simulation (DNS2) uses Method 2 for inflow turbulence, and the length scale of the most energy containing eddies in the inflow turbulence is in the “attached amplifying” regime. Table 4 shows numerical parameters used in the simulations, and Figure 26 shows the schematic diagram of the simulation domain.

$N_x, N_y, N_z, L_x, L_y$  and  $L_z$  represent the number of grid points in  $x, y$  and  $z$  directions, and the respective domain lengths;  $L_E$  denotes the domain length of the Exit Zone;  $l$  represents length scale of the inflow turbulence at the energy peak;  $\delta$  is 99% laminar boundary layer thickness;  $v'/v_{inflow}$  is the free-stream turbulence intensity; Reynolds number based on  $\delta$  is

240; Mach number based on free-stream conditions is 0.4; Prandtl number is 0.72; an ideal gas is assumed with constant specific heat ( $\gamma = 1.4$ ) for both simulations. No-slip condition and the isothermal condition,  $T_w/T_\infty = 0.8$  are used at the wall. The non-reflecting boundary condition is imposed at the inflow and outflow boundaries. Both simulations were performed up to a nondimensional time of 2.3 where time is normalized by flow turn-over time ( $\tau$ ) which represents approximately the time taken for the flow to reach from the inflow boundary to the edge of the boundary layer.

Figure 27(a) shows the surface contours of the streamwise vorticity for DNS1. The contours in the upper plane show the streamwise vorticity near the inflow boundary whereas the contours in the lower plane show elongated streamwise vorticity stretched in the  $x$  direction near the wall. The temperature field also has elongated contours near the wall. Figure 27(b) shows the surface contours of the streamwise vorticity for DNS2. Again, elongated streamwise vorticity in the  $x$  direction is noted. However, the surface contours in the lower plane appear more complicated. Some contours are also aligned in the  $z$  direction, which are not seen in Figure 27(a). This suggests that the flow field in DNS2 is more three-dimensional.

Since DNS1 is in the “damping” regime, the streamwise vorticity is damped from the inflow boundary to the wall whereas the streamwise vorticity in DNS2 is amplified. This results in qualitatively different temperature fields. Figure 28(a) shows contours of the temperature field at  $x = 0$  in  $y-z$  plane for DNS1. The temperature field is disturbed mildly due to the damped streamwise vorticity, and the skin friction and wall heat transfer are mildly affected. The temperature field for DNS2 shown in Figure 28(b) is more disturbed due to the amplified streamwise vorticity. The temperature contours are similar to the mushroom-like temperature contours in Figure 12. Figure 29(a) shows the contours of  $St$  at the wall for DNS1. It shows stretched contours similar to Figure 27(a). Evidently, even though the streamwise vorticity is damped, it affects the structure of the temperature gradient at the wall. Figure 29(b) shows the contours of  $St$  for DNS2. The contours appear to be streaky in  $x$  direction, but are wider and varying in  $z$  direction.

To study the response of  $C_f$  and  $St$  to the free-stream turbulence,  $C_f$  and  $St$  averaged over the spanwise direction are plotted against time for both cases. The response of the skin friction at three different streamwise locations for DNS1 is viewed in Figure 30(a). The horizontal axis represents the time normalized by  $\tau$  (the flow turn-over time), and the vertical axis is the percent change of  $C_f$  from the initial value. There is a transition period when the initial inflow turbulence is convected from the inflow boundary to the boundary layer. After this transition period, a statistically stationary state is approached. The transition period ends around non-dimensional time of 0.4. After the transition,  $\Delta C_f$  fluctuates around a mean value of 10%. Figure 30(b) is the same plot for DNS2. Unlike the Figure 30(a),  $\Delta C_f$  fluctuates around a mean value of 19% at  $x = 6.6\delta$ . The mean change in  $\Delta C_f$  is 13% at  $x = 11.1\delta$ . For DNS2, the curves fluctuates more at all  $x$  locations than curves in Figure 30(a). Figure 31(a) shows time history of  $St$  for DNS1. The vertical axis is  $\Delta St$  (in percent) from the laminar value. There is also a transition period for the wall heat transfer, and it ends around non-dimensional time of 1.0. After the transition,  $\Delta St$  fluctuates around a mean value of 25%, which is higher than the mean value for  $\Delta C_f$ . Figure 31(b) is the

same plot for DNS2. The  $\Delta St$  fluctuates around a mean value of 70% at  $x = 0.1\delta$ , 60% at  $x = 6.6\delta$  and 55% at  $x = 11.1\delta$ , respectively after the transition period. This confirms that  $St$  is more sensitive to the free-stream turbulence than  $C_f$  as found in the simulations of the organized inflow disturbances. Interestingly, the  $C_f$  curves show more fluctuations than the  $St$  curves.

Turbulence statistics were collected for both simulations. It should be emphasized that all DNS results are preliminary and averaging over longer time is needed to reduce the statistical fluctuations. The turbulence statistics for DNS1 are nearly converged whereas the turbulence statistics for DNS2 are not converged for the mean  $u$  velocity and turbulent kinetic energy. Other higher order statistics for DNS2 will be obtained in the near future. Preliminary statistics from DNS2 are included in this report.

Mean profiles of  $u$  velocity and temperature for both cases are compared with laminar profiles. The mean  $u$  velocity profiles are shown in Figure 32(a). Curve for DNS2 shows more deviation from the laminar profile near the edge of the laminar boundary layer ( $\eta = 2.4$ ), and consequently higher gradient at the wall. The same trend is preserved for mean temperature curve shown in Figure 32(b). Curve for DNS2 has more deviation and higher gradient at the wall. It should be noted that these plots show only a small part of the calculation domain. At larger distance from the wall, the velocity and temperature profiles do return to the free-stream values.

The three components of turbulent kinetic energy were obtained. Figure 33, 34 and 35 show the variation of the  $\overline{u'^2}$ ,  $\overline{v'^2}$  and  $\overline{w'^2}$  respectively at three different  $x$  locations for both DNS1 and DNS2, against the self-similar coordinate,  $\eta$ . The turbulent kinetic energy is normalized by  $q_o^2$  where  $\frac{1}{2}q_o^2$  is the turbulent kinetic energy at  $x = 0$  in the inflow boundary. Figure 33(a) shows that  $\overline{u'^2}$  for DNS1 decays monotonically from the inflow boundary. Figure 33(b) shows that  $\overline{u'^2}$  for DNS2 decays, but values obtained at each  $x$  are higher for all  $\eta$  than DNS1. Figure 34(a) shows that  $\overline{v'^2}$  for DNS1 has a region of a constant value, and then decays to the wall. On the other hand,  $\overline{v'^2}$  for DNS2 have significantly different trend, which is shown in Figure 34(b). Since DNS2 is in "attached amplifying" regime, the streamwise vorticity is amplified, and so is  $\overline{v'^2}$ . The curves of  $\overline{v'^2}$  have a transition region from the inflow boundary where the curves decay, and then rise to peak values near  $\eta = 6$ . After reaching the peak values, the curves decay to zero at the wall. This trend has been observed in experiments (Sadeh et al, 1970). Figure 35(a) shows that  $\overline{w'^2}$  for DNS1 decays monotonically from the inflow boundary, but increases near the wall before going to zero at the wall. Figure 35(b) shows the variation of  $\overline{w'^2}$  for DNS2 at three different  $x$  locations. Curves have similar trend to Figure 35(a), but have significantly higher values. The peak value associated with DNS1 at  $x = 0.1\delta$  is 0.05 approximately whereas the peak value with DNS2 at the same  $x$  location is 0.5. This confirms the fact that the velocity field is significantly disturbed by the inflow turbulence. Figure 36(a) shows the variation of the turbulence kinetic energy at three different  $x$  location along  $\eta$ . The curves at three different  $x$  locations decay from the inflow boundary toward the wall. This is attributed to the fact that the length scale of the inflow turbulence is in the "damping" regime. The turbulent kinetic energy with DNS2 is plotted in Figure 36(b). It is evident that the turbulent kinetic energy has nondimensional value of

0.5 from  $\eta = 2$  to  $\eta = 20$  approximately, and then rises to the value at the inflow boundary. Similar trend for the turbulent kinetic energy was observed by numerical calculations with turbulence models. (Traci & Wilcox, 1975; Wang & Yeh, 1988)

Figure 37(a) shows the rms temperature fluctuations,  $\sqrt{t'^2}$  along  $\eta$  at three different  $x$  locations for DNS1. The temperature fluctuations are confined to a small region inside boundary layer. Figure 37(b) shows the variation of  $\sqrt{t'^2}$  for DNS2. It shows a higher peak value of approximately 0.17, which occurs at  $\eta = 1.5$  roughly the location of the peak in DNS1. Figure 38(a) shows  $\overline{v't'}$  versus  $\eta$  for DNS1. All curves have negative values, and the maximum value has a peak value -0.007 at  $\eta = 2$ . Figure 38(b) shows  $\overline{v't'}$  for DNS2. It shows the larger peak heat flux magnitude and the broader distribution of the heat flux across the boundary layer.

## 5 Conclusions

A Summary of the key conclusions from the work described in this report follows.

- A new code with the option of using a fourth order central differencing scheme or an optimized scheme with the same 5 point stencil in the evaluation of the spatial derivatives, and second order implicit time advancement scheme was developed. The optimized scheme represented the high wave number better than the fourth order central differencing scheme, and allows significant savings in the computational cost.
- A method suitable for prescribing realistic inflow turbulence in the DNS of stagnation point flow which uses non-uniform meshes was developed. The statistics showed that the homogeneity and the isotropy are maintained in the center of the domain where the grid size in  $x$  direction is comparable to the grid size in  $y$  and  $z$  directions.
- The simulations of stagnation point flow conducted with organized inflow disturbances confirmed the existence of the neutral scale. The streamwise vorticity is amplified if the spanwise length scale of inflow disturbance is larger than the neutral scale.
- Three length scale regimes are identified: "damping" regime, "attached amplifying" regime and "detached amplifying" regime. The enhancement is correlated with the length scale for "damping" and "attached amplifying" regimes whereas the enhancement is inversely correlated with the length scale for "detached amplifying" regime. "Attached amplifying" regime is the most effective in the enhancement of the skin friction and wall heat transfer.
- $St$  was shown to be more sensitive to the organized disturbances than  $C_f$ . The heat transfer enhancement is found to be 4-5 times the skin friction enhancement.
- The higher the intensity of the organized disturbances, the larger is the enhancement of the skin friction and wall heat transfer. The enhancement saturates with large length scale.



- The qualitative dependence of Reynolds number and spanwise length scale observed with the organized inflow disturbances is consistent with the experimental findings in the turbulent flow regime.
- DNS of stagnation point flow with moderate grid resolution shows that  $C_f$  and  $St$  are enhanced by the free-stream turbulence by 10% and 25% respectively for the case of DNS1 and around 20% and 70% respectively for the case of DNS2.
- Mean profiles of  $u$  velocity and temperature for DNS2 show deviations from laminar profiles, resulting in higher shear and temperature gradient at the wall. The turbulent kinetic energy was found to decay from the inflow boundary to the wall for the case of DNS1. On the other hand, preliminary turbulent statistics for the case of DNS2 show that the  $\overline{v'^2}$  increases from the free-stream to the edge of the boundary layer.
- Work will be continued, focusing on DNS of stagnation point flow with fine grid resolution.

## 6 Acknowledgement

The computer time for the simulations was provided by NAS supercomputers at NASA Ames research center. We acknowledge the financial support from the Air Force Office of Scientific Research, Air Force Material Command, USAF, under grant number AFOSR-91-0198-D.

## References

- [1] Simonich, J. C. & Bradshaw, P., Effect of free-stream turbulence on heat transfer through a turbulent boundary layer, *J. of Heat Transfer* (1978), vol. 100, pp 671-677.
- [2] Hancock, P.E. & Bradshaw, P., The Effects of Free Stream Turbulence on Turbulent Boundary Layers, *Journal of Fluid Engineering* (1983), vol. 105, pp 284-289.
- [3] Kestin, J., The effect of free-stream turbulence on Heat transfer rates, *Advances in Heat Transfer* (1966), vol. 3, pp 1-32.
- [4] Sutera, S. P., Vorticity amplification in stagnation-point flow and its effect on heat transfer, *J. of Fluid Mechanics* (1965), vol.21, pp 513-534.
- [5] Ames, F. E. & Moffat, R. J., Heat transfer with high intensity, large scale turbulence: The flat plate turbulent boundary layer and the cylindrical stagnation point, Report No. HMT-43, Stanford University, 1990.
- [6] Ames F. E., Experimental study of vane heat transfer and aerodynamics at elevated levels of turbulence, NASA contractor report No. 4633, 1994.

- [7] Traci, R. M. & Wilcox, D. C., Freestream turbulence effects on stagnation point heat transfer, AIAA J. (1975), vol. 13, no. 7, pp 890-896.
- [8] Blair, M. F., Influence of free-stream turbulence on turbulent boundary layer heat transfer and mean profile development, PartI-Experimental data, J. of Heat transfer (1983), vol. 105, pp 33-40.
- [9] Blair, M. F., Influence of free-stream turbulence on turbulent boundary layer heat transfer and mean profile development, PartII-Analysis of results, J. of Heat transfer (1983), vol. 105, pp 41-47.
- [10] Giles, M., Non-reflecting boundary conditions for the Euler equations, CFDL-TR-88-1, 1988.
- [11] Colonius, T., Lele, S. K. & Moin, P., Boundary conditions for direct computation of aerodynamic sound generation, AIAA J. (1993), vol. 31, pp 1574-1582.
- [12] VanFossen, G. J., Simoneau, R. J. & Ching, C. Y., Influence of turbulence parameters, Reynolds number and body shape on stagnation region heat transfer, J. of Heat transfer (1995), vol. 117, pp 597-603.
- [13] Sadeh, W. Z., Suter, S. P. & Maeder, P. F., An investigation of vorticity amplification in stagnation flow, ZAMP, vol. 21, pp 717-742.
- [14] Wang, C. R. & Yeh, F. C., Application of turbulence modeling to predict surface heat transfer in stagnation flow region of circular cylinder, NASA TP-2758, 1987.
- [15] Sabry, A. S. & Liu, J. T. C., Longitudinal vorticity elements in boundary layers: non-linear development from initial Görtler vortices as a prototype problem, J. of Fluid Mechanics (1991), vol. 231, pp 615-663.
- [16] Suter, S. P., Maeder P. F. & Kestin, J., On the sensitivity of heat transfer in the stagnation-point boundary layer to free-stream vorticity, J. of Fluid Mechanics (1963), vol. 16, pp 497-520.
- [17] Champion, M. & Libby, P., Stagnation Streamline turbulence Revisited, AIAA (1990), vol28, No 8, pp 1525-1526.
- [18] Castro, I. P., Effects of Free Stream Turbulence on Low Reynolds Number Boundary Layers, ASME Journal of Fluid Engineering (1984), vol. 106, pp 298-306.
- [19] VanFossen, G. J. & Simoneau, R. J., A study of the relationship between free-stream turbulence and stagnation region heat transfer, J. of Heat transfer (1987), vol. 109, pp 10-24.
- [20] Lele, S. K., Compact finite difference schemes with spectral-like resolution. J. of Comp. Phy. (1992), vol. 103, pp 16-42.

- [21] Eibeck, P. A. & Eaton, J. K., Heat transfer effects of a longitudinal vortex embedded in a turbulent boundary layer, *J. Heat Transfer* (1987), vol. 109, pp 16-24.
- [22] Saric, W.S., Görtler vortices, *Annual Review on Fluid Mechanics* (1994), vol. 26, pp 379-409.
- [23] Malan, P., Heat transfer in shear-free turbulent boundary layers, Ph.D thesis, Stanford University, 1993.
- [24] Bott, D., Free-stream turbulence effects on the turbulent boundary layers, Ph.D thesis, Stanford University, 1996.
- [25] Perot, J. B., Shear-free turbulent boundary layers: physics and modelling, Ph.D thesis, Stanford University, 1993.

Case	Grid Points	Differencing Scheme	$Re_{\lambda_0}$
Scheme 1	$80^3$	Sixth order compact scheme	25
Scheme 2	$80^3$	Fourth order central differencing scheme	25
Scheme 3	$120^3$	Fourth order central differencing scheme	25
Scheme 4	$80^3$	Optimized scheme	25

Table 1: Schemes tested on isotropic turbulence decay.

Experiment	$l/D$	$Re_D$	$Re_\delta$	$l/\delta$
Van Fosssen et al. (1995)	0.05-0.3 (integral length scale)	37,000-228,000	230-570	8-119
Ames (1990)	1-10 (dissipation length scale)	19,000	170	114-1140

Table 2: The ranges of length scales associated with inflow turbulence used in recent experiments.

Case	$\lambda_{org}/\delta$	$A_{org}$	$Re_\delta$	$Re_L$	$\overline{\Delta C_f}$	$\overline{\Delta St}$	$H_v$	$H_s$	$L_v$	$H_m$	$v'_m/(S\delta)$	$w'_m/(S\delta)$	$t'_m/\Delta T$
L2I05	2.1(*)	0.05	170	5000	0.0067	0.035	N/A	N/A	N/A	12.4	0.17	0.030	0.011
L2I10	2.1(*)	0.10	170	5000	0.061	0.25	N/A	N/A	N/A	12.4	0.33	0.060	0.022
L2I25	2.1(*)	0.25	170	5000	0.43	1.7	N/A	N/A	N/A	12.4	0.84	0.15	0.054
L3I05	3.2	0.05	170	5000	0.21	0.91	2.3	N/A	3.8	3.3	0.25	0.15	0.050
L3I10	3.2	0.10	170	5000	0.80	3.6	2.3	2.0	3.6	3.4	0.50	0.29	0.095
L3I25	3.2	0.25	170	5000	4.1	20	2.5	4.8	3.3	3.5	1.3	0.73	0.17
L4I05	4.0	0.05	170	5000	0.34	1.5	2.2	N/A	4.5	3.2	0.30	0.23	0.068
L4I10	4.0	0.10	170	5000	1.3	6.0	2.2	2.7	4.2	3.2	0.61	0.45	0.13
L4I25	4.0	0.25	170	5000	5.7	28	2.7	5.5	3.5	3.5	1.6	1.1	0.19
L5I05	5.3	0.05	170	5000	0.33	1.6	2.2	N/A	5.6	3.4	0.31	0.29	0.073
L5I10	5.3	0.10	170	5000	1.2	6.3	2.3	3.0	4.9	3.4	0.62	0.59	0.13
L5I25	5.3	0.25	170	5000	5.3	28	3.2	6.0	3.6	3.8	1.7	1.4	0.18
L5I25R2	5.3	0.25	240	10000	11	50	5.6	9.6	4.4	5.5	5.1	2.6	0.20
L7I25R2	7.4	0.25	240	10000	7.0	35	5.8	9.6	4.4	5.6	3.5	2.6	0.19
L9I25R2	9.3	0.25	240	10000	5.5	28	5.9	9.6	4.4	5.7	2.9	2.6	0.18
L10I25R2	10.6	0.25	240	10000	4.8	24	6.1	9.6	4.5	6.0	2.7	2.6	0.17
L5I25R3	5.3	0.25	340	20000	14	65	6.6	12	4.6	6.4	7.3	3.4	0.22
L10I25R3	10.6	0.25	340	20000	6.8	28	11	17	7.3	11	11	5.1	0.19

Table 3: Tables of parameters used for DNS with organized disturbances. Overall parameters deduced from the simulation are also given.  $\overline{\Delta C_f}$  and  $\overline{\Delta St}$  are in terms of percent increase relative to the laminar value.  $H_v$ ,  $H_s$ ,  $L_v$  and  $H_m$  are given in terms of the similarity variable (note that the 99% laminar boundary layer thickness is 2.4 in these units.)

Case	Nx	Ny	Nz	$L_x$	$L_y$	$L_z$	$L_E$	$l/\delta$	$v'/v_{inflow}$	Regime
DNS1	191	128	64	$25\delta$	$6.25\delta$	$5\delta$	$7\delta$	2.5	0.05	damping
DNS2	95	96	64	$25\delta$	$10\delta$	$11.7\delta$	$4\delta$	2.9	0.25	attached amplifying

Table 4: The numerical parameters of DNS.

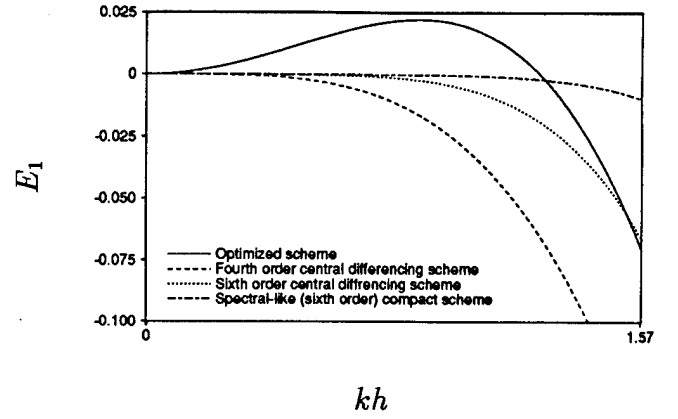
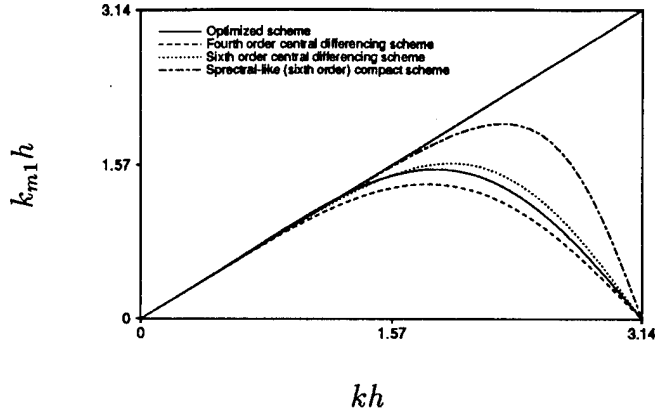


Figure 1: (a): The modified wave number  $k_{m1}$  for first derivative schemes (left). (b): Error in the modified wave number,  $E_1 = (k_{m1} - k)/k$  for first derivative schemes (right)

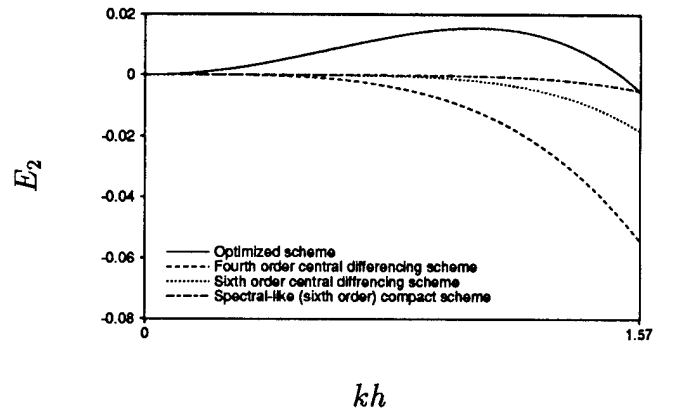
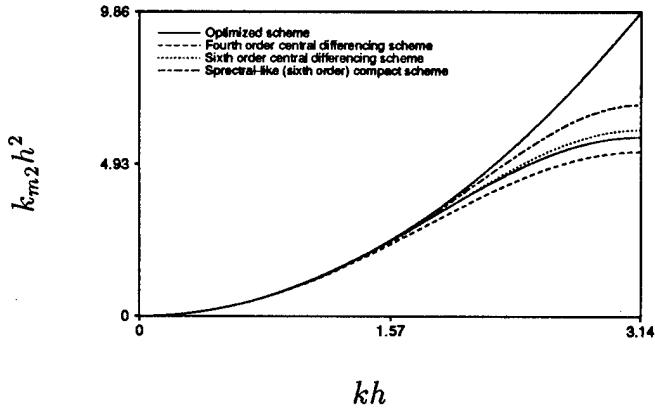


Figure 2: (a): The modified wave number  $k_{m2}$  for second derivative schemes (left). (b): Error in the modified wave number,  $E_2 = (k_{m2} - k^2)/k^2$ .

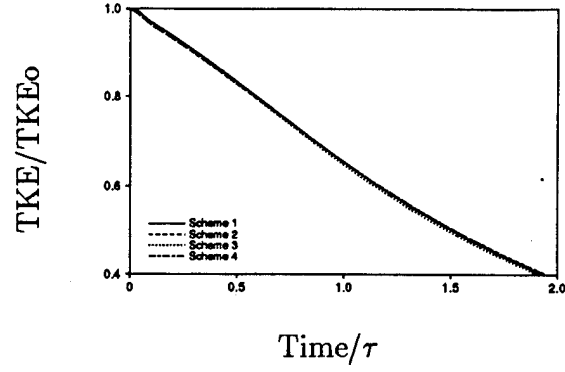


Figure 3: Turbulent kinetic energy decay for different numerical schemes.

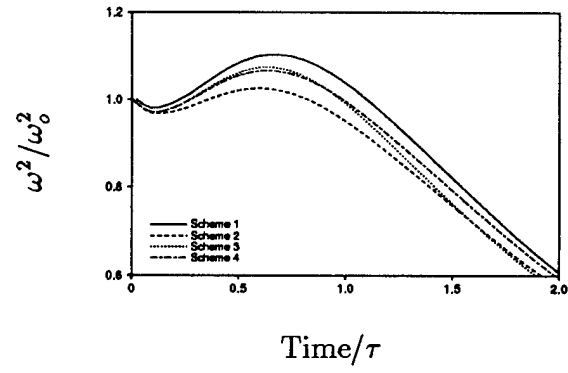


Figure 4: Vorticity evolution for different numerical schemes.

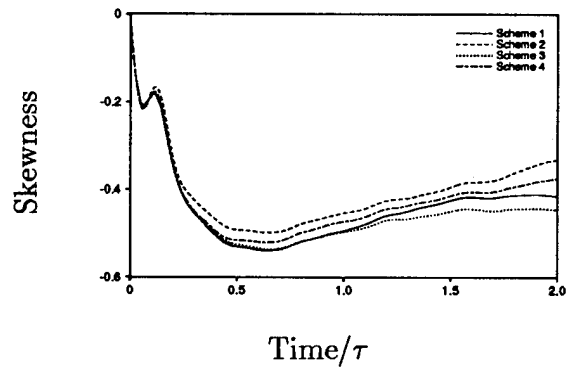


Figure 5: Velocity derivative skewness for different numerical schemes.

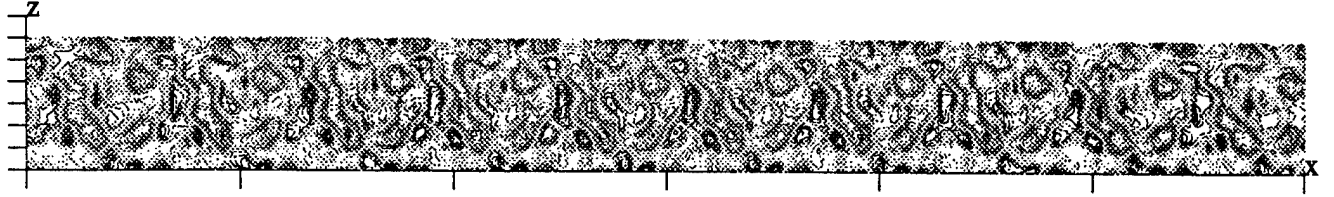


Figure 6: The  $w$  velocity in  $x - z$  plane at the inflow boundary from a moderate resolution DNS of stagnation point flow with inflow turbulence provided using Method 1.  $x = 0$  at the center of domain, and the increment of tic marks in  $x$  coordinate is  $8.3\delta$  ( $\delta$  is the 99% laminar boundary layer thickness.) The  $z$  coordinate varies from 0 to  $5\delta$  and the increment of tic marks is  $0.83\delta$ .

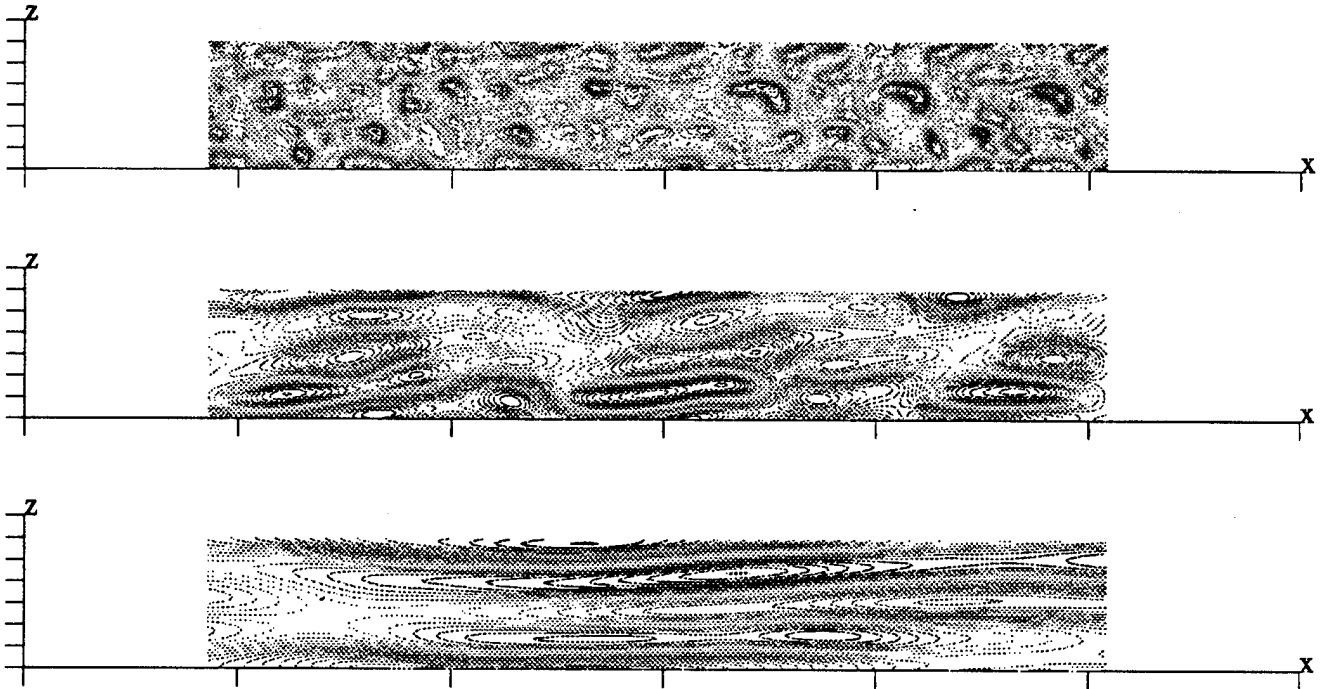


Figure 7: The evolution of the streamwise vorticity in moderate resolution DNS of the stagnation point flow with inflow turbulence provided using Method 1. The top  $x - z$  contours are sampled at  $y = 6\delta$  where  $\delta$  is the .99 laminar boundary layer thickness; The middle  $x - z$  contours are sampled at  $y = 3\delta$ ; The bottom  $x - z$  contours are sampled at  $y = 0.5\delta$ .  $x = 0$  at the center of domain, and the increment of tic marks in  $x$  coordinate is  $8.3\delta$ . The  $z$  coordinate varies from 0 to  $5\delta$  and the increment of tic marks is  $0.83\delta$ .



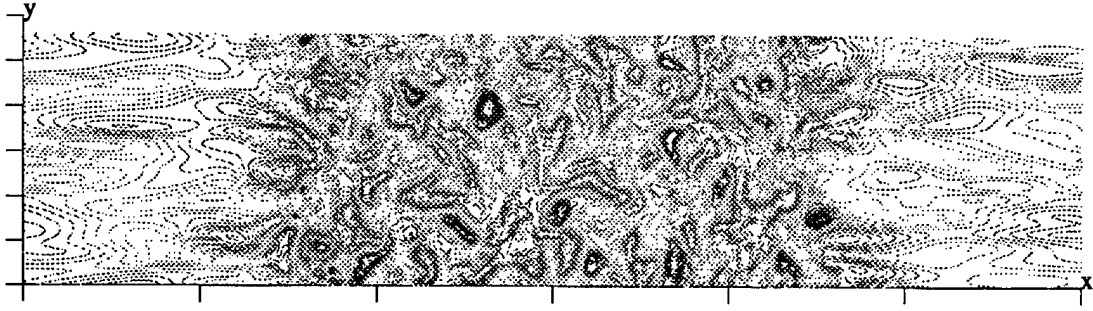


Figure 8: The  $w$  velocity in  $x - y$  plane for the simulation of the homogeneous and isotropic turbulence to generate the inflow turbulence by Method 2.  $x = 0$  at the center of domain, and the increment of tic marks in  $x$  coordinate is  $8.3\delta$ . The  $z$  coordinate varies from 0 to  $12.5\delta$  and the increment of tic marks is  $2.08\delta$ .

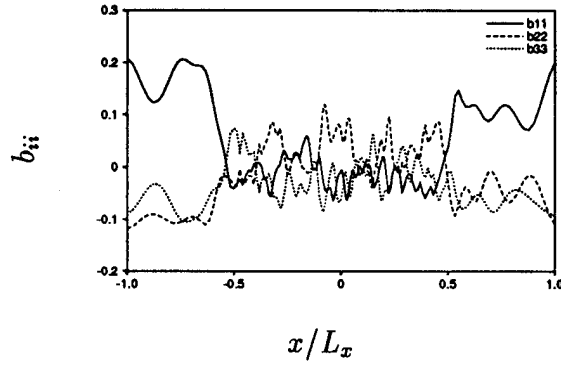


Figure 9: The variation of normal Reynolds stress anisotropy  $b_{ii}$  with  $x$ .  $L_x$  is the domain size.

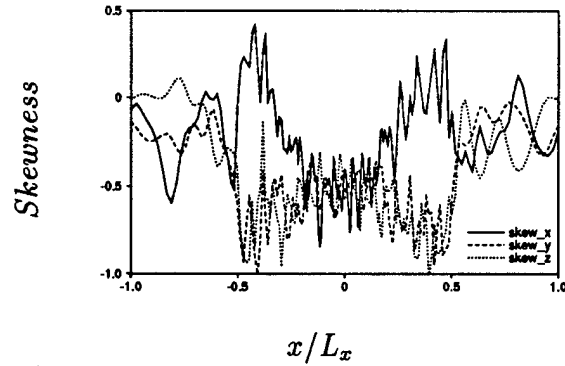


Figure 10: The variation of velocity derivative skewness with  $x$ .  $L_x$  is the domain size.

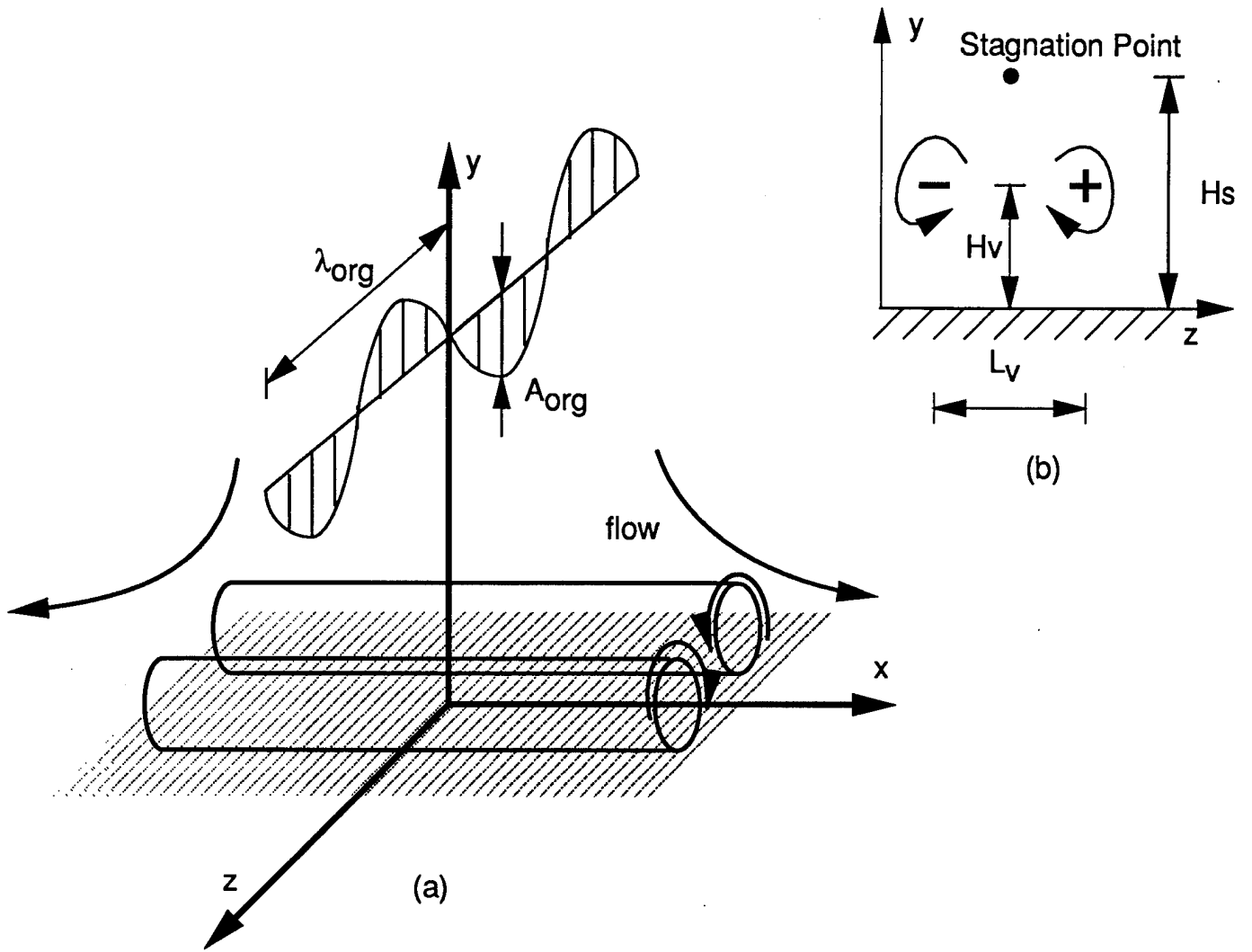


Figure 11: (a): The schematic diagram of simulations with organized disturbances. (b): The schematic diagram of counter-rotating vortices.

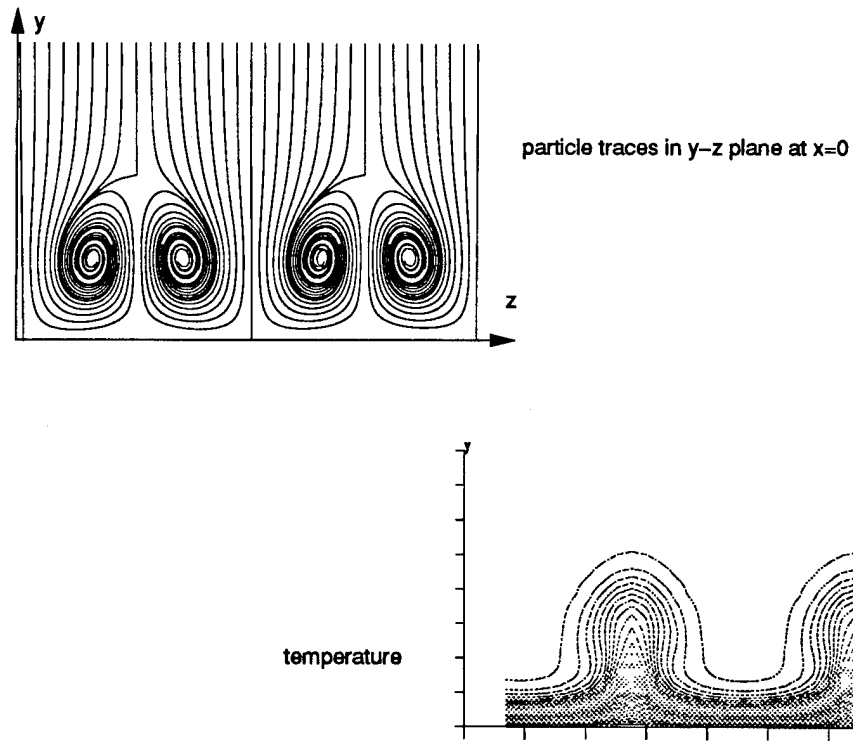


Figure 12: The particle traces and the temperature contours in  $y - z$  plane for the case of L5I25. The  $y$  coordinate varies from 0 to  $7.5\delta$  and the increment of tic marks is  $0.83\delta$ . The  $z$  coordinate of temperature contours varies from 0 to  $11.8\delta$  and the increment of tic marks is  $1.5\delta$ . The contours levels have a minimum of 0.8 at the wall ( $y=0$ ) and the maximum of 1.0 with the contour increment, 0.01.

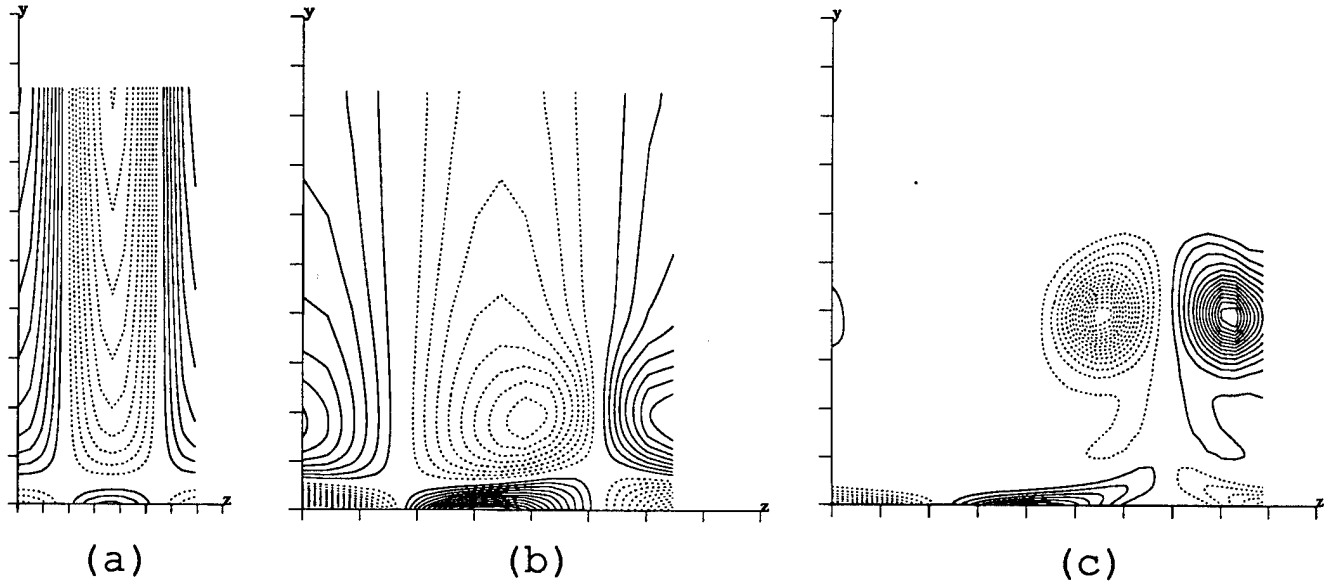


Figure 13: The contours of streamwise vorticity. (a) L2I25, (b) L4I25, (c) L10I25R3. Solid lines represent positive values and dotted lines represent negative lines. (a) contours vary from -1.4 to 1.4 with the increment of 0.14. (b) contours vary from -3.4 to 3.4 with the increment of 0.34. (c) contours vary from -18 to 18 with the increment of 1.8.

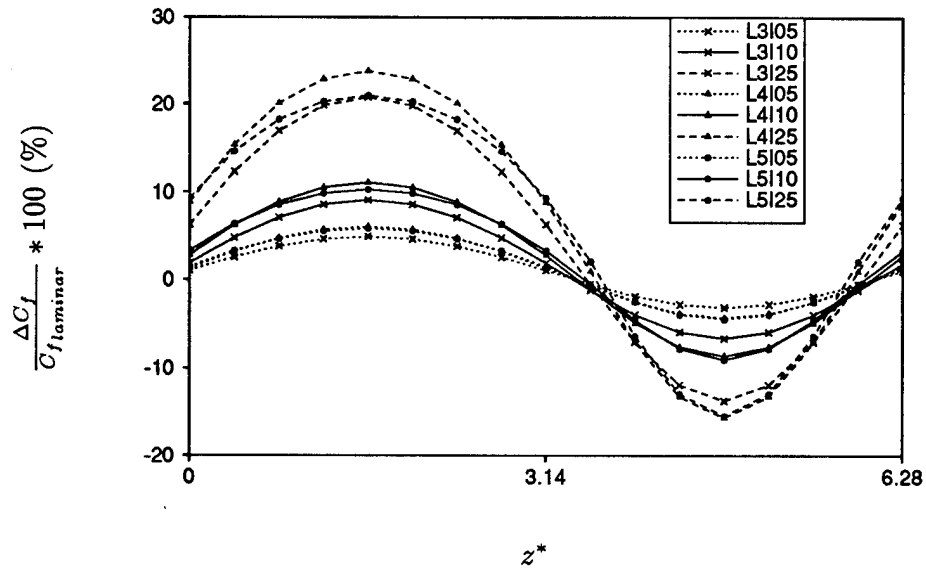


Figure 14: The plot of the deviation of  $C_f$  from its laminar value in the spanwise direction.  $z^*$  is defined as  $2\pi z / \lambda_{org}$ .

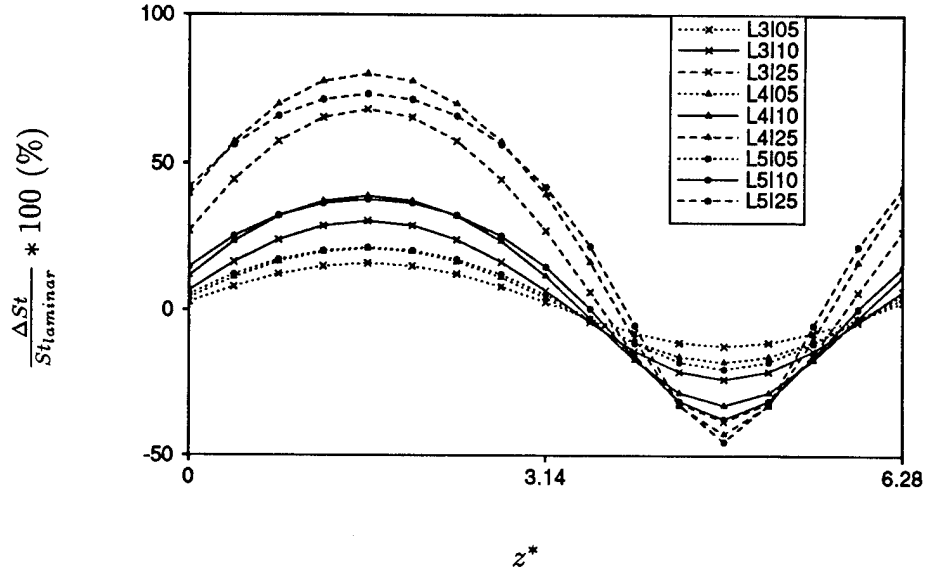


Figure 15: The plot of the deviation of  $St$  from its laminar value in the spanwise direction.  $z^*$  is defined as  $2\pi z/\lambda_{org}$ .

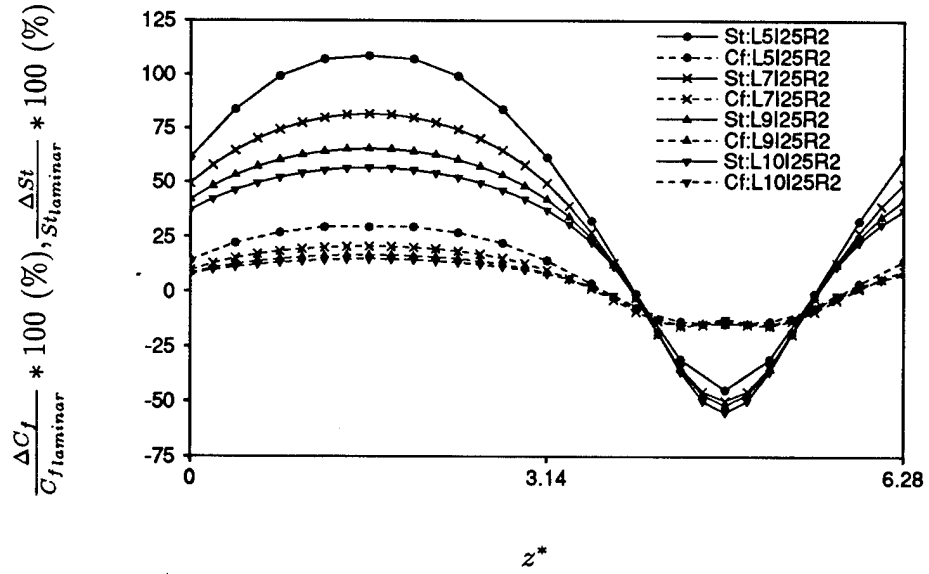


Figure 16: The plot of the deviation of  $C_f$  and  $St$  from its laminar value in the spanwise direction with a fixed intensity, 25% and Reynolds number,  $Re_\delta = 240$ .  $z^*$  is defined as  $2\pi z/\lambda_{org}$ .

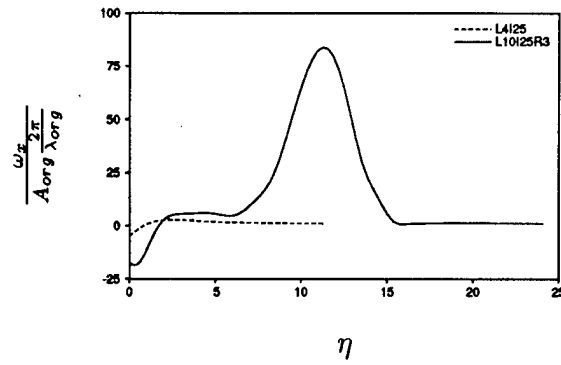


Figure 17: The variation of the streamwise vorticity along the self-similar coordinate,  $\eta$ ; dashed line: case L4I25; solid line: case L10I25R3.

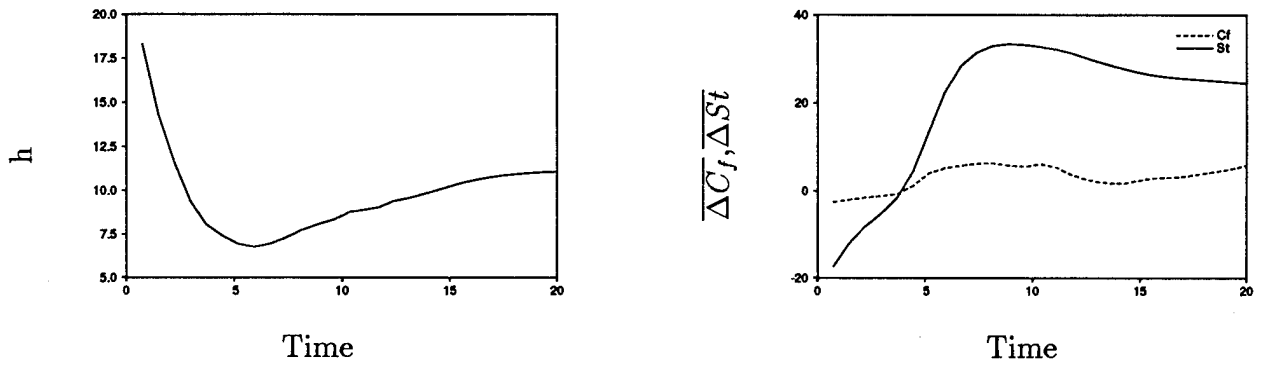


Figure 18: The time evolution of (a) the distance of peak vorticity from the wall ( $h$ ) (left) and (b) percent values of  $\overline{\Delta C_f}$  and  $\overline{\Delta St}$ .

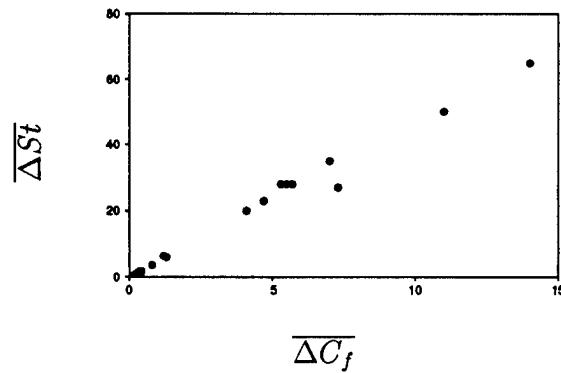


Figure 19: A cross-plot of the percent changes  $\overline{\Delta C_f}$  vs.  $\overline{\Delta St}$  for all cases.

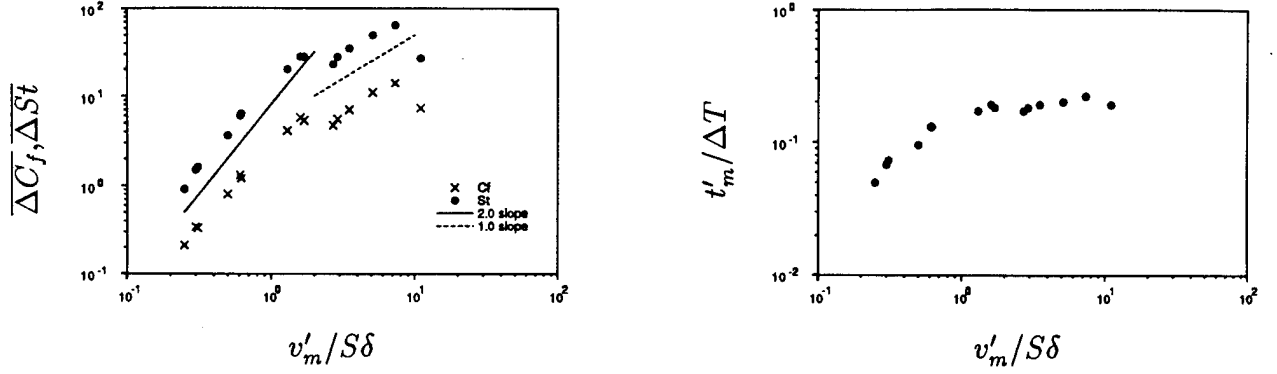


Figure 20: (a):  $v'_m/S\delta$  vs.  $\Delta C_f(\%)$  and  $\Delta St(\%)$  (left). (b):  $v'_m/S\delta$  vs.  $t'_m/\Delta T$  (right).

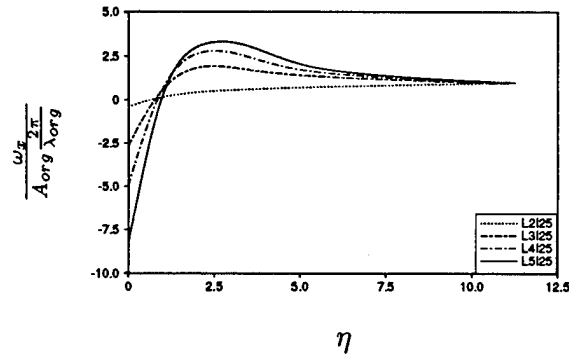


Figure 21: The variation of the streamwise vorticity with 25% intensity along the self-similar coordinate,  $\eta$ .

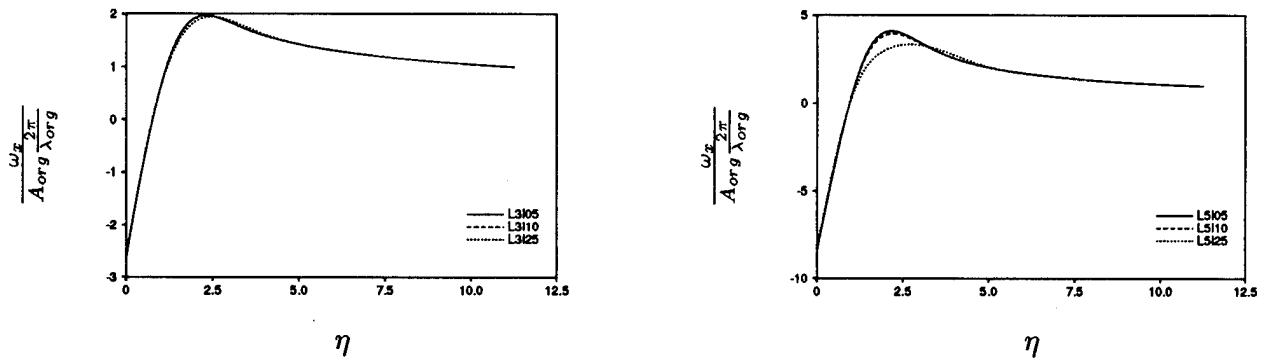


Figure 22: The variation of the streamwise vorticity with the length scale of (a)  $3.2\delta$  (left) and (b)  $5.3\delta$  (right) along the self-similar coordinate,  $\eta$ .

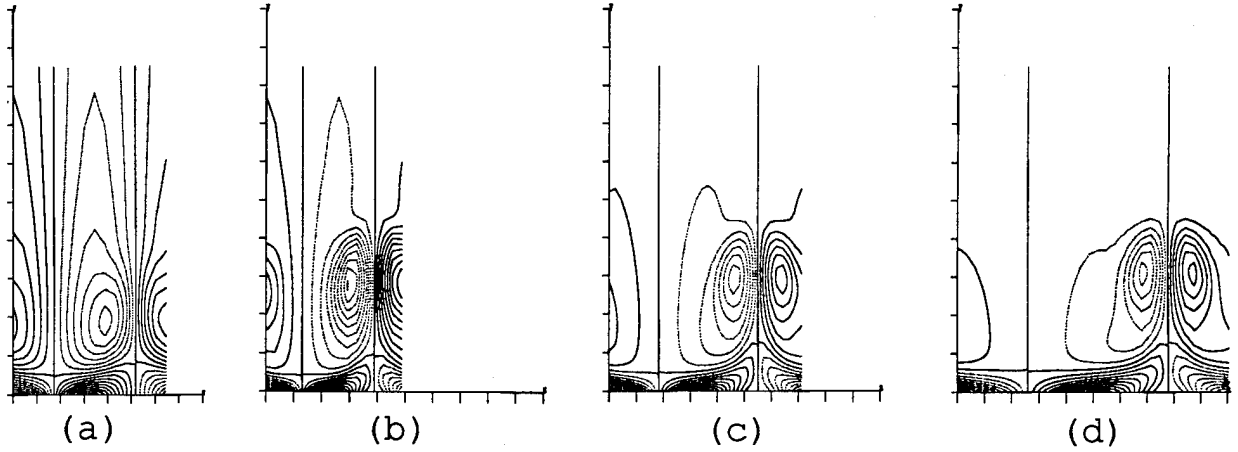


Figure 23: The contours of streamwise vorticity. (a) L4I25, (b) L5I25R2, (c) L7I25R2, (d) L10I25R2. Solid lines represent positive values and dotted lines represent negative lines. (a) contours vary from -3.4 to 3.4 with the increment of 0.34. (b) contours vary from -7.2 to 7.2 with the increment of 0.72. (c) contours vary from -6.7 to 6.7 with the increment of 0.67. (d) contours vary from -6.0 to 6.0 with the increment of 0.60. The  $y$  coordinate varies from 0 to  $5.9\delta$  with tic marks at  $0.59\delta$  for (a), and from 0 to  $8.3\delta$  with tic marks at  $0.83\delta$  for (b) (c) and (d). The  $z$  coordinate varies from 0 to  $4.5\delta$  with tic marks at  $0.55\delta$  for (a), and from 0 to  $10.4\delta$  with tic marks at  $1.04\delta$  for (b), (c) and (d).

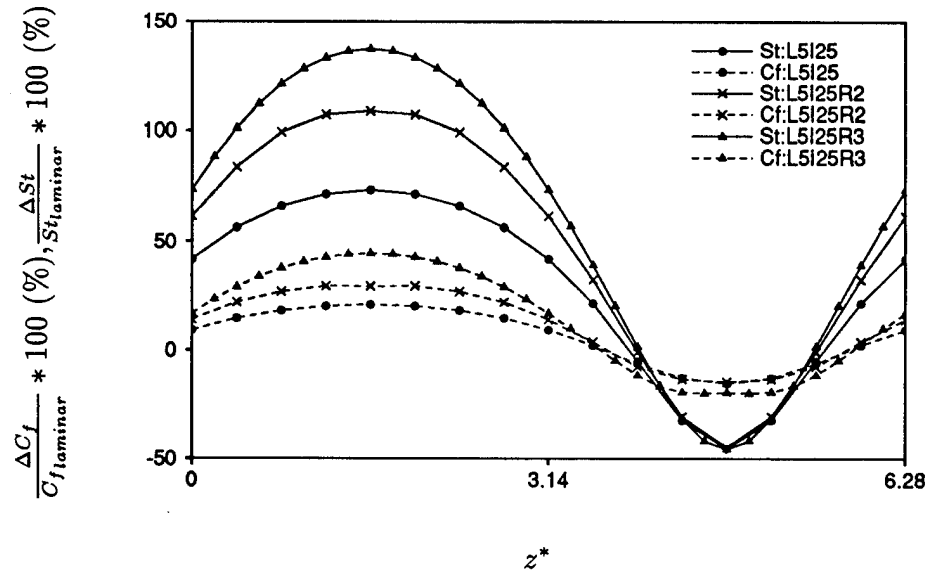


Figure 24: The plot of  $\Delta C_l$  and  $\Delta St$  against the spanwise direction for different Reynolds number and a fixed length scale,  $5.3\delta$  and fixed intensity, 25%.  $z^*$  is defined as  $2\pi z / \lambda_{org}$



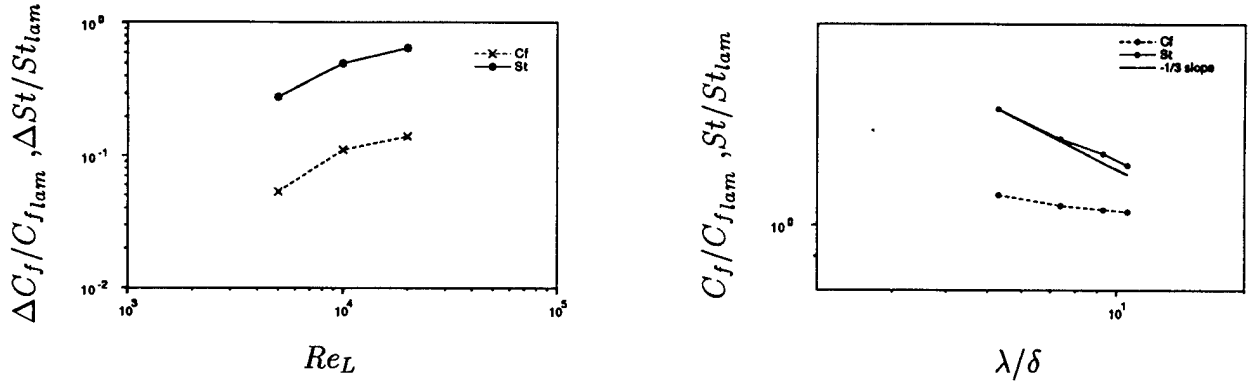


Figure 25: (a):  $\Delta C_f/C_{f_{lam}}$  and  $\Delta St/St_{lam}$  vs.  $Re_L$  (left). (b):  $C_f/C_{f_{lam}}$  and  $St/St_{lam}$  vs. the spanwise length scale (right). The subscript *lam* means laminar value. The slope for *St* curve in (a) is 0.37.

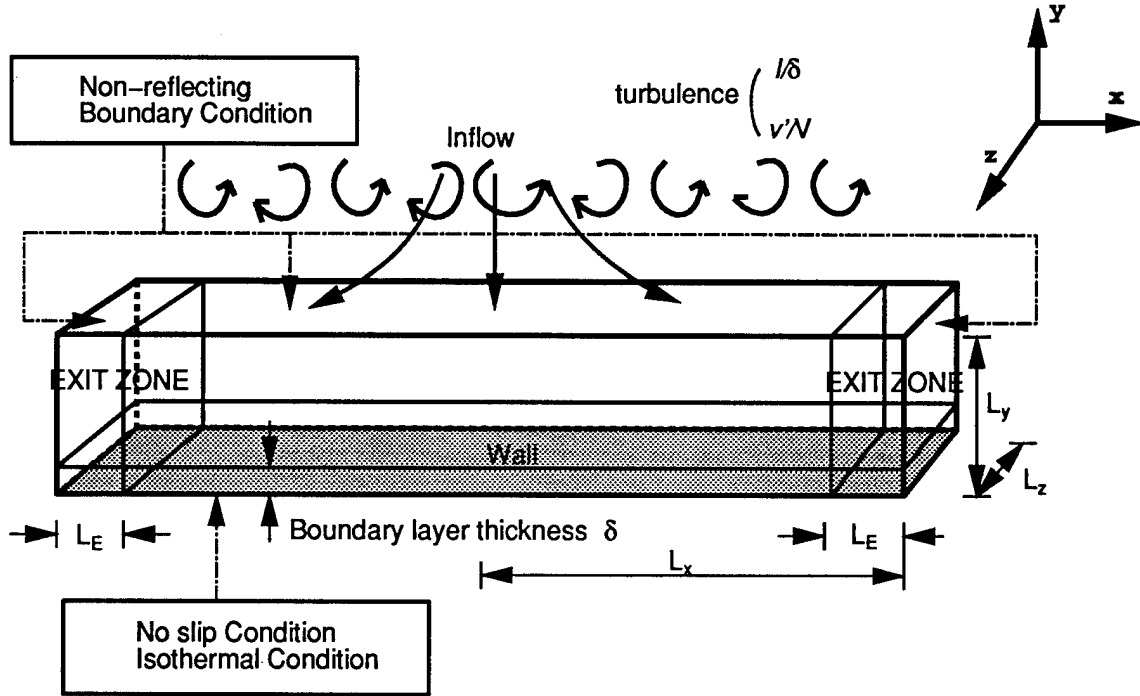
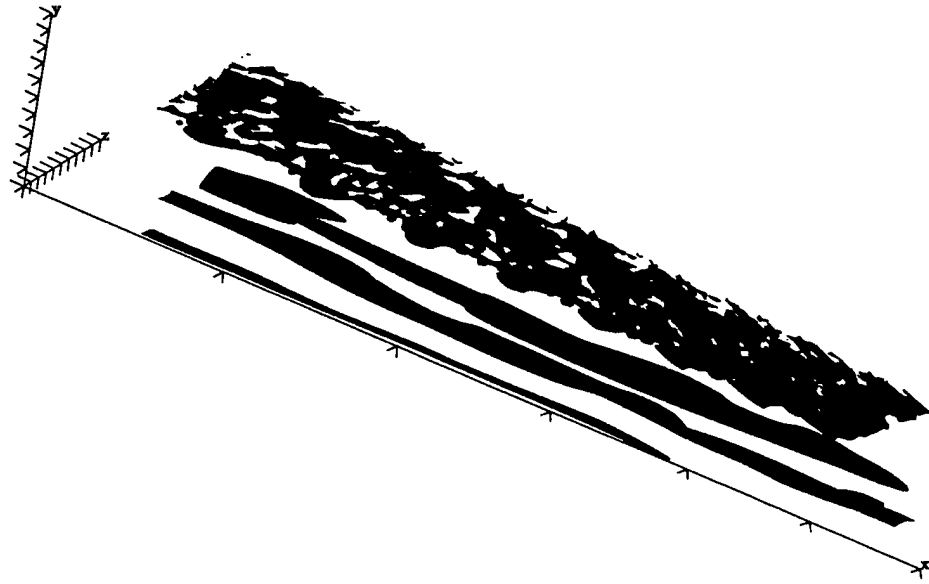
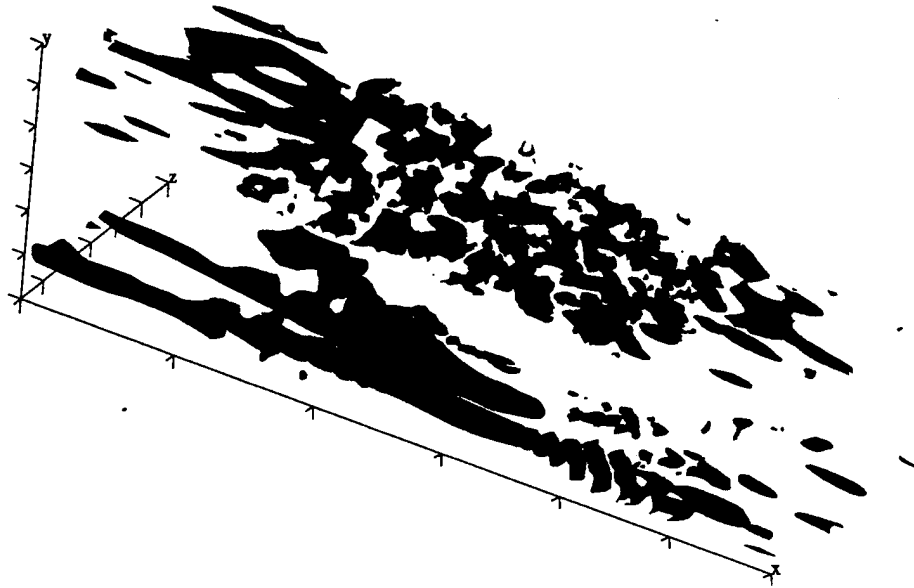


Figure 26: The schematic diagram of DNS domain.



(a)



(b)

Figure 27: The surface contours of the streamwise vorticity for (a) DNS1 and (b) DNS2. The contours in upper plane show small scale streamwise vorticity near the inflow boundary. The contours in the lower plane show elongated streamwise vorticity stretched in  $x$  direction near the wall. The contour level is  $0.32 q_0/\delta$  for (a) and  $0.72 q_0/\delta$  for (b) where  $\frac{1}{2}q_0^2$  is the turbulent kinetic energy at  $x = 0$  at the inflow boundary.

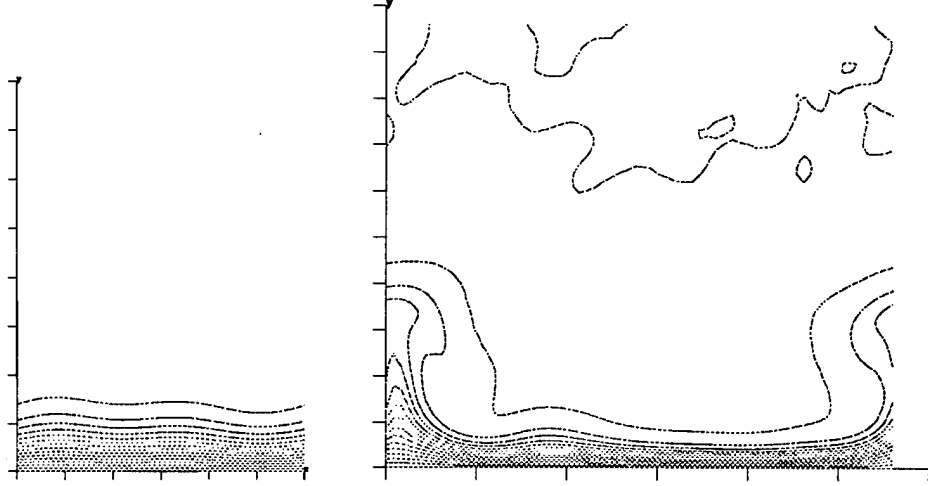


Figure 28: The contours of temperature field in  $y - z$  plane at  $x = 0$  for (a) DNS1 (left) and (b) DNS2 (right). The  $y$  coordinate varies from 0 to  $7.5\delta$  with tic marks at  $0.83\delta$  for (a), and from 0 to  $12.5\delta$  with tic marks at  $1.04\delta$  for (b). The  $z$  coordinate varies from 0 to  $5\delta$  with tic marks at  $0.83\delta$  for (a), and from 0 to  $12.5\delta$  with tic marks at  $2.08\delta$  for (b). The contours has the minimum of 0.8 at the wall ( $y=0$ ) and the maximum of 1.0 with the increment of contour, 0.01 for both (a) and (b).

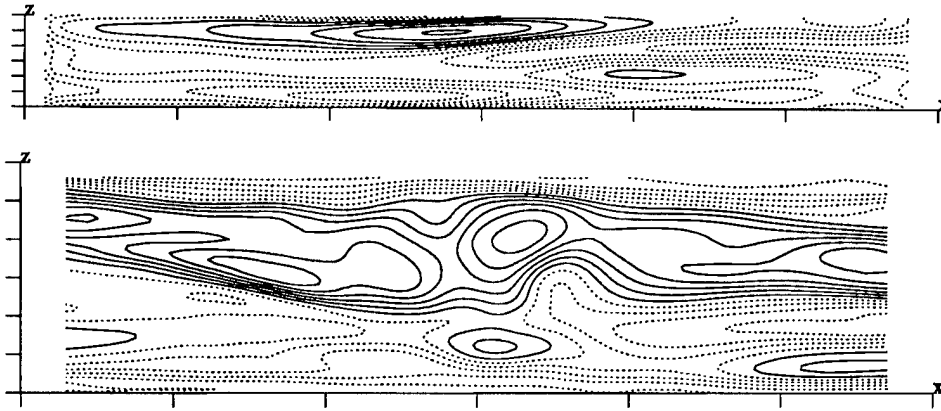


Figure 29: The contours of  $St$  at the wall for (a) DNS1 (above) and (b) DNS2 (below). The  $x$  coordinate varies from  $-25\delta$  to  $25\delta$  and the increment of tic marks is  $8.3\delta$  for both (a) and (b). The  $z$  coordinate varies from 0 to  $5\delta$  with tic marks at  $0.83\delta$  for (a), and from 0 to  $12.5\delta$  with tic marks at  $2.08\delta$  for (b). (a): The dotted line varies from 0.0064 to 0.0076 with the increment of contour, 0.0002, and the solid line varies from 0.0078 to 0.0088 with the same increment. (b): The dotted line varies from 0.002 to 0.008 with the increment of contour, 0.001, and the solid line varies from 0.009 to 0.015 with the same increment.

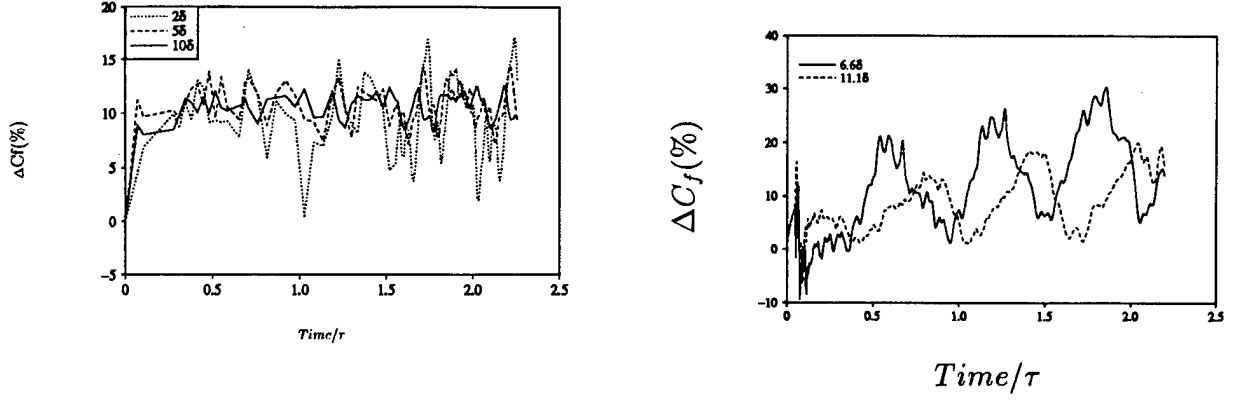


Figure 30: The time history of the change of  $C_f$  from its initial value for (a) DNS1 (left) and (b) DNS2 (right).

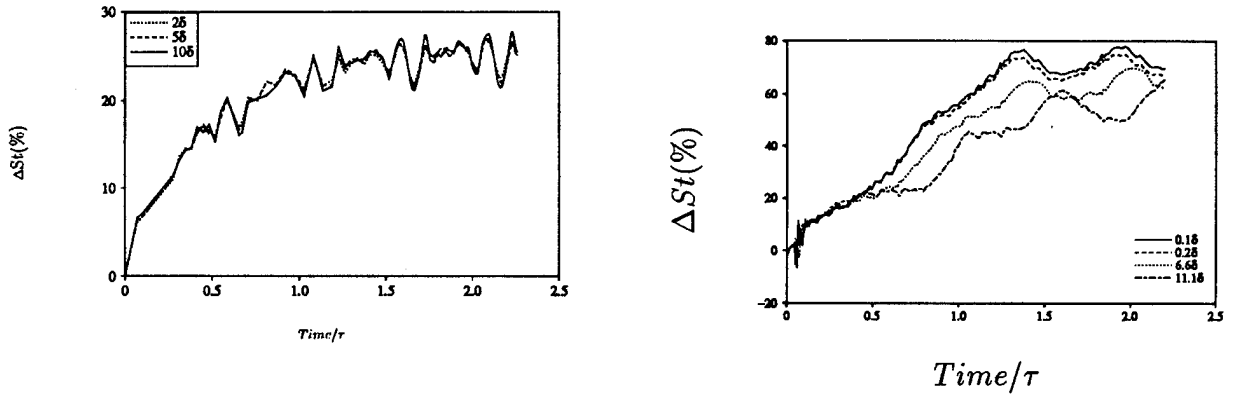


Figure 31: The time history of the change of  $St$  from its initial value for (a) DNS1 (left) and (b) DNS2 (right).

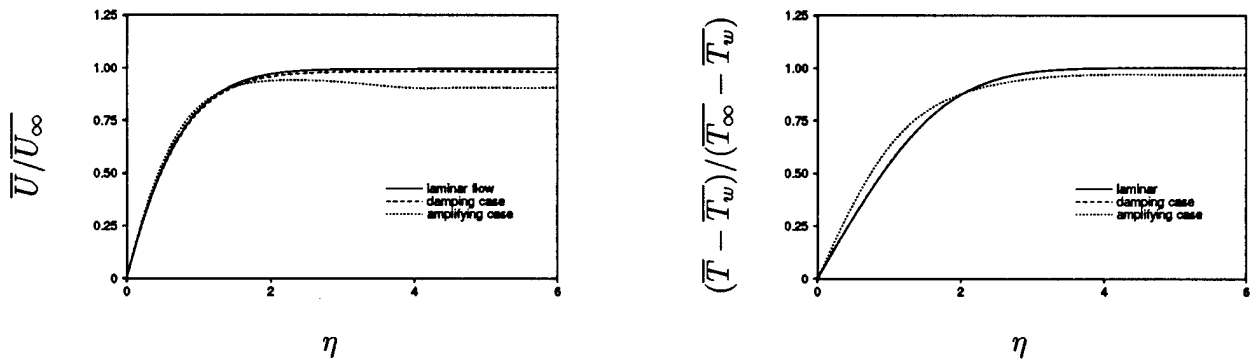


Figure 32: The variation of (a) mean  $u$  velocity (left) and (b) mean temperature (right) along the self-similar coordinate,  $\eta$  at  $x = 6.6\delta$  for DNS1 and DNS2.

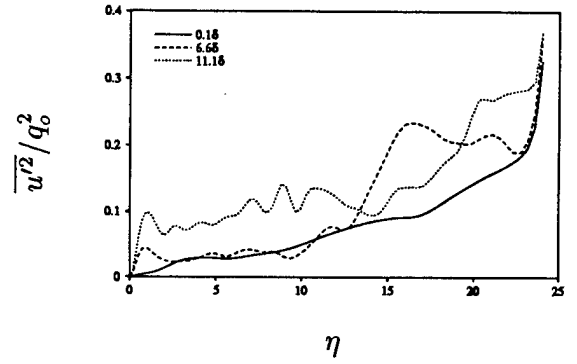
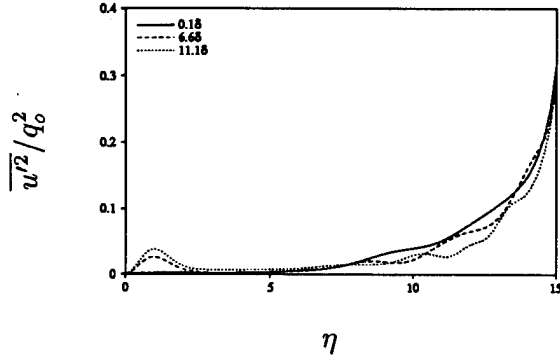


Figure 33: The variation of  $\overline{u'^2}/q_o^2$  along the self-similar coordinate,  $\eta$  at three different  $x$  locations for (a) DNS1 (left) and (b) DNS2 (right).

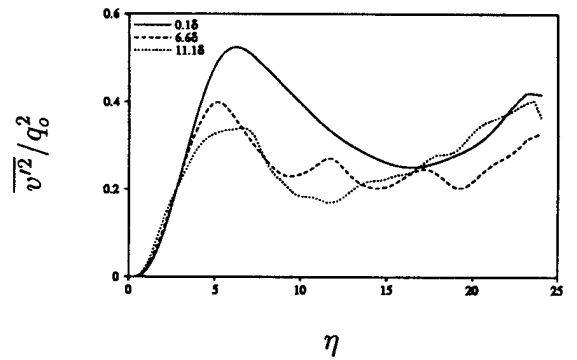
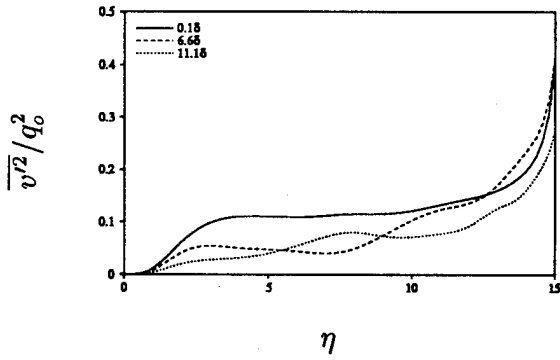


Figure 34: The variation of  $\overline{v'^2}/q_o^2$  along the self-similar coordinate,  $\eta$  at three different  $x$  locations for (a) DNS1 (left) and (b) DNS2 (right).

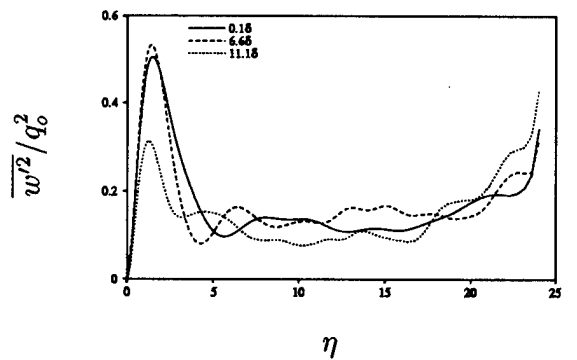
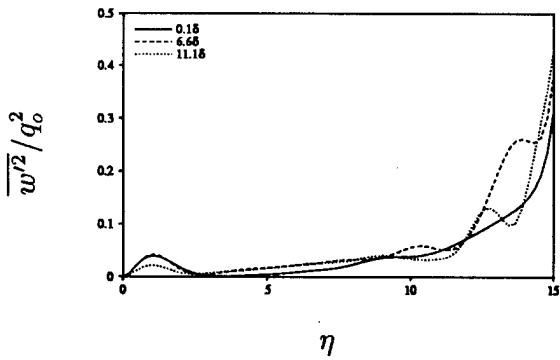


Figure 35: The variation of  $\overline{w'^2}/q_o^2$  along the self-similar coordinate,  $\eta$  at three different  $x$  locations for (a) DNS1 (left) and (b) DNS2 (right).

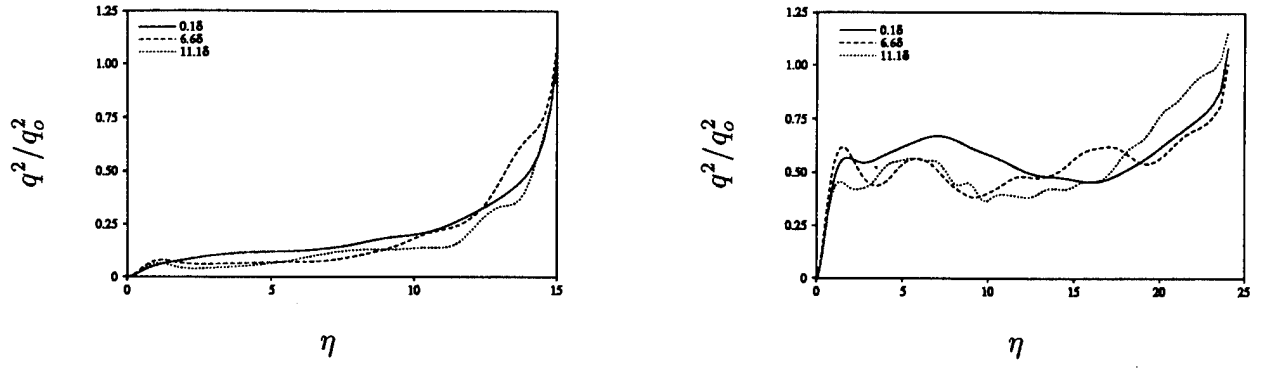


Figure 36: The variation of  $q^2/q_0^2$  along the self-similar coordinate,  $\eta$  at three different  $x$  locations for (a) DNS1 (left) and (b) DNS2 (right).  $q^2 = \overline{u'^2} + \overline{v'^2} + \overline{w'^2}$ .

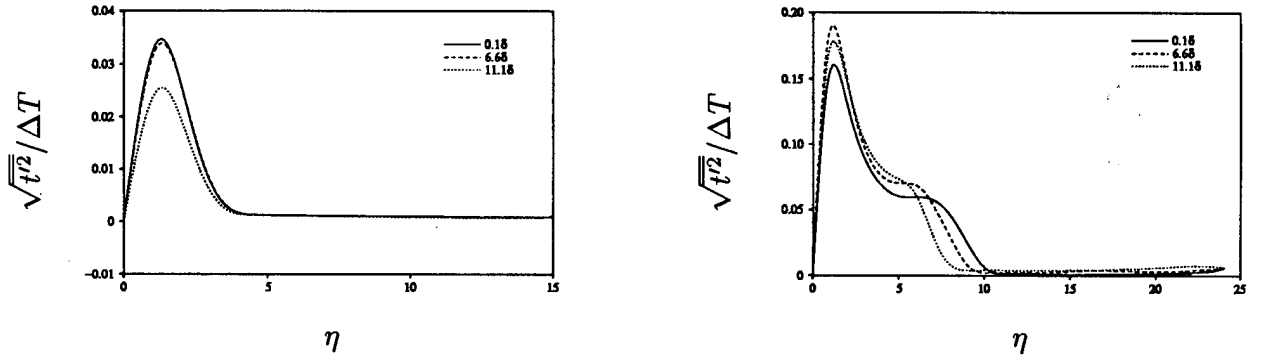


Figure 37: The variation of rms temperature fluctuations along the self-similar coordinate,  $\eta$  at three different  $x$  locations for (a) DNS1 (left) and (b) DNS2 (right).

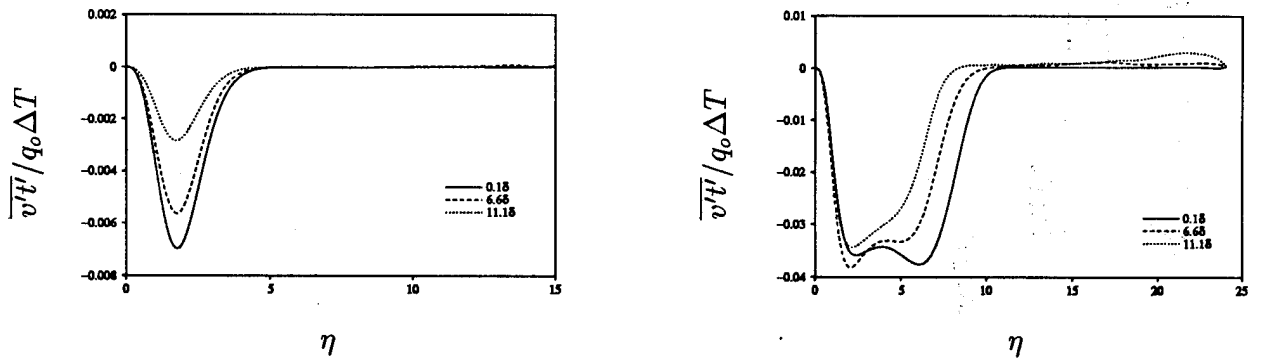


Figure 38: The variation of  $\overline{v't'}/q_0\Delta T$  along the self-similar coordinate,  $\eta$  at three different  $x$  locations for (a) DNS1 (left) and (b) DNS2 (right).